ESAT-6 undergoes self-association at phagosomal pH and an ESAT-6 specific nanobody restricts M. tuberculosis growth in macrophages

Timothy A Bates[1], Mila Trank-Greene[1], Xammy Nguyenla[1], Aidan Anastas[1], Sintayehu Gurmessa[1], Ilaria R Merutka[1], Shandee D Dixon[1], Anthony Shumate[2], Matthew AH Parson[3], Jessica R Ingram[4], Eric Barklis[1], John E Burke[3,5], Ujwal Shinde[2], Hidde L Ploegh[4], Fikadu G Tafesse[1,6]

[1]Department of Molecular Microbiology and Immunology, Oregon Health & Sciences University, Portland, Oregon, United States.

[2]Department of Chemical Physiology and Biochemistry, Oregon Health & Science University, Portland, Oregon, United States.

[3]Department of Biochemistry and Microbiology, University of Victoria, Victoria, Canada.

[4]Program in Cellular and Molecular Medicine, Boston Children's Hospital, Harvard Medical School, Boston, Massachusetts, United States.

[5]Department of Biochemistry and Molecular Biology, The University of British Columbia, Vancouver, Canada.

[6]Correspondence to tafesse@ohsu.edu

Abstract

Mycobacterium tuberculosis (Mtb) is known to survive within macrophages by compromising the integrity of the phagosomal compartment in which it resides. This activity primarily relies on the ESX-1 secretion system, predominantly involving the protein duo ESAT-6

and CFP-10. CFP-10 likely acts as a chaperone, while ESAT-6 likely disrupts phagosomal membrane stability via a largely unknown mechanism. we employ a series of biochemical analyses, protein modeling techniques, and a novel ESAT-6-specific nanobody to gain insight into the ESAT-6's mode of action. First, we measure the binding kinetics of the tight 1:1 complex formed by ESAT-6 and CFP-10 at neutral pH. Subsequently, we demonstrate a rapid self-association of ESAT-6 into large complexes under acidic conditions, leading to the identification of a stable tetrameric ESAT-6 species. Using molecular dynamics simulations, we pinpoint the most probable interaction interface. Furthermore, we show that cytoplasmic expression of an anti-ESAT-6 nanobody blocks Mtb replication, thereby underlining the pivotal role of ESAT-6 in intracellular survival. Together, these data suggest that ESAT-6 acts by a pH dependent mechanism to establish two-way communication between the cytoplasm and the Mtb-containing phagosome.

Introduction

Tuberculosis (TB), caused by *Mycobacterium tuberculosis* (Mtb), is a major global health concern, claiming over 1.6 million lives annually. Mtb is highly adept at evading the immune system, and it can persist within an infected person for decades. This situation is worsened by the nearly 1.7 billion people globally who harbor a dormant Mtb infection (Houben and Dodd, 2016), coupled with the rising trend of drug-resistant TB cases (World Health Organization, 2022).

To successfully establish an infection in the host, Mtb utilizes a plethora of virulence factors delivered via its several ESX-secretion systems. Studies have indicated that Mtb has the ability to damage the phagosomal membrane, a process that is heavily reliant on the activity of the ESX-1 secretion system (Conrad et al., 2017; López-Jiménez et al., 2018; Schnettger et al., 2017). Currently, the most probable candidate driving ESX-1 dependent lytic activity is the well-known T cell antigen, the 6 kDa early secreted antigenic target (ESAT-6, or EsxA)) (Andersen et al., 1995;

46 Sørensen et al., 1995), after which the ESX family of T7SSs was originally named (Gey van Pittius
47 et al., 2001). Secretion of the various ESX-1 substrates are known to be highly complex and
48 interdependent, and while the full scope of ESX-1 components and substrates is still being worked
49 out, many individual ESX-1 component knockouts are known to phenocopy the ESAT-6 deletion,
50 indicating that ESAT-6 itself is responsible for the lion's share of the activity (Chen et al., 2012;
51 Clemmensen et al., 2017; Cronin et al., 2022; Lienard et al., 2020; Sanchez et al., 2020).

52 Over the last few decades, there have been numerous studies focused on uncovering the
53 possible mechanism of membrane lysis by ESAT-6 (Augenstreich et al., 2020; Conrad et al., 2017;
54 de Jonge et al., 2007; Kinhikar et al., 2010; Koo et al., 2008; Lienard et al., 2020; Osman et al.,
55 2022), and how this might lead to escape of Mtb from the phagosome (Houben et al., 2012).
56 However, the field has been plagued by setbacks such as the discovery that many studies prior
57 to 2017 showing membrane disruption by ESAT-6 were confounded by the contamination with the
58 detergent ASB-14, which was originally added to remove endotoxin (Conrad et al., 2017).
59 Consequently, most recent studies have focused on the use of intact bacteria in assays, frequently
60 with the closely related *Mycobacterium marinum* (Mm), to avoid using recombinant proteins. The
61 conclusions of these experiments are complicated by the interdependent nature of ESX-1
62 structural components, chaperones, and substrates (Augenstreich et al., 2020; Osman et al.,
63 2022; Santucci et al., 2022). Mm has been a valuable model for working out ESX-1 and ESAT-6
64 function, and many of the key studies in the field have used Mm exclusively. However, the unique
65 characteristics of Mm compared to Mtb can sometimes leads to differing results, and conclusions
66 drawn from one species do not always apply to the other (Bosserman et al., 2019; Carlsson et
67 al., 2009; Lienard et al., 2020; Osman et al., 2022; Smith et al., 2008). This is important because
68 the membranolytic activity of the ESX-1 seems to be highly context dependent, and more
69 biochemical work is needed to work out the specific contributions of ESAT-6 to the membrane
70 disruption phenotype.

71 Despite extensive research, the precise mechanism of ESAT-6 action remains elusive.
72 This study aims to bridge this gap by performing comprehensive biochemical and cellular
73 investigations of ESAT-6 under neutral and acidic conditions. We use biolayer interferometry (BLI)
74 to measure the tight association between ESAT-6 and CFP-10, and the pH dependent ESAT-6
75 self-association. We use fluorescence microscopy to directly observe formation of large ESAT-6
76 complexes, and we measure the stoichiometry of ESAT-6 under different pH conditions using
77 multi-angle light scattering. We then use molecular dynamics-based modeling to evaluate the
78 most likely modes of ESAT-6 interaction. We also generated a novel ESAT-6-binding alpaca-
79 derived nanobody, E11rv, to further define the significance of ESAT-6 during Mtb infection. We
80 perform biochemical characterization of E11rv, as well as functional testing, which showed
81 inhibition of Mtb growth inside macrophages treated with E11rv or expressing cytoplasmic E11rv.

82 Results

83 Recombinant ESAT-6 and CFP-10 purification

84 In seeking to perform functional studies of ESAT-6 and CFP-10, we produced recombinant
85 protein using *E. coli* expression plasmids available from BEI Resources: pMRLB.7 (NR-50170)
86 containing ESAT-6, and pMRLB.46 (NR-13297) containing CFP-10. Both of these plasmids have
87 been used extensively in literature, including many of the most influential biochemical
88 characterization studies (Augenstreich et al., 2020; Behura et al., 2019; Chen et al., 2019; Choi
89 et al., 2010; Conrad et al., 2017; de Jonge et al., 2007; Eitson et al., 2012; Gallegos et al., 2008;
90 Harrison et al., 2014; Koyuncu et al., 2021; Lim et al., 2016; Mukherjee et al., 2007; Niazi et al.,
91 2015; Osman et al., 2022; Pathak et al., 2007; Peng et al., 2011; Refai et al., 2015; Smith et al.,
92 2008; Stavri et al., 2012; Vesosky et al., 2010; Woolhiser et al., 2007; Xiao et al., 2016; Yang et
93 al., 2008). The specification sheet for pMRLB.7 indicates that it includes a C-terminal FALE
94 solubility tag and subsequent Histidine affinity tag while pMRLB.46 indicates that it contains only

95 a C-terminal Histidine tag. We performed sequencing of both plasmids (Figs 1A and S1), and
96 noticed a stretch of 10 additional amino acids ahead of the reported tags in the pMRLB.7 plasmid.
97 The precise amino acid sequence of the pMRLB.46 plasmid has not been reported, but it appears
98 to contain 4 additional amino acids ahead of the expected tag. Importantly, we were able to
99 confirm that the full and complete sequences of ESAT-6 and CFP-10 are each contained in their
100 respective plasmids, and the inconsistencies fall within the C-terminal tag regions of each protein
101 (Figs 1A and S1).

102 Expression and purification by Nickel-NTA chromatography resulted in bands of the
103 expected sizes by SDS-PAGE and His_6-specific western blot (Fig 1B). Amino acid sequences of
104 the recombinant proteins were also confirmed by mass spectrometry (MS), where it was observed
105 that CFP-10 undergoes N-terminal methionine excision in our *E. coli* expression system (Fig S2)
106 (Giglione et al., 2004; Hirel et al., 1989). Size exclusion chromatography (SEC) showed
107 appropriate relative retention volumes and combining equimolar quantities of ESAT-6 with CFP-
108 10 resulted in a leftward shift, suggesting correct dimerization (Fig 1C).

109 Dimerization of ESAT-6 and CFP-10 at neutral pH

110 To validate that ESAT-6 and CFP-10 are forming a native dimer, we next performed native-
111 PAGE with different ratios of the two proteins (Fig 2A). We incubated ESAT-6 and CFP-10 for 1
112 hour at 4°C prior to running the gels, combining them in different ratios. The isoelectric point of
113 ESAT-6 and CFP-10 are both quite low, for our constructs they are 5.18 (net charge -8.22 at pH
114 7.4) and 5.72 (net charge -5.27 at pH 7.4), respectively. Thus, we oriented the positive electrode
115 toward the bottom of the gel. As expected, we observed that ESAT-6 ran faster than CFP-10.
116 Combinations of each showed a distinct third band of intermediate charge which was greatest in
117 the 1:1 mixture and absent in each pure protein, indicating formation of a 1:1 complex with no
118 intermediate species. This aligns with our results from Fig 1C, and aligns with historical research

119 on the interaction between ESAT-6 and CFP-10 (Poulsen et al., 2014; Renshaw et al., 2005,
120 2002).

121 Another commonly used test of ESAT-6 function is hemolysis, or the ability to damage red
122 blood cell (RBC) membranes and release hemoglobin. Historical studies reported that ESAT-6
123 was able to cause hemolysis, but Conrad et al. discovered that most of this hemolytic activity was
124 due to detergent contamination with ASB-14, which is commonly added during the wash steps of
125 Nickel-NTA purification to remove endotoxin (Conrad et al., 2017). Our recombinant ESAT-6 was
126 produced without detergent, and we confirmed that it was not able to induce hemolysis at any pH
127 between 4.5 and 7.5 (Fig S3). However, the hemolysis assay still finds contemporary use when
128 testing the ability of whole bacteria to induce membrane damage in an ESX-1 and contact-
129 dependent manner (Augenstreich et al., 2020; Bosserman et al., 2019; Conrad et al., 2017;
130 Osman et al., 2022). In such experiments, RBCs are mixed with log-phase bacterial cultures at
131 high MOI and pelleted by centrifugation to force direct contact. Similar to previous reports, we
132 found that *Mycobacterium marinum* (Mm) is capable of efficiently causing hemolysis within 2
133 hours (Fig 2B). In contrast, we found that Mtb was incapable of hemolysis over a similar time
134 frame. It is well established that Mm-induced hemolysis is ESX-1 dependent, but our results
135 suggest that there are some differences in Mtb that affect the rate or extent of hemolysis. One
136 previous study was able to induce hemolysis using Mtb, but this required 48 hours instead of the
137 typical 2 (Augenstreich et al., 2020).

138 Binding kinetics of ESAT-6 and CFP-10

139 To measure the binding strength of ESAT-6 and CFP-10 we developed a biolayer
140 interferometry (BLI) assay to measure their interactions (Fig 3A). We first measured the ability of
141 ESAT-6 and CFP-10 to form homo-oligomers or hetero-oligomers (Fig 3B), and found that they
142 preferentially formed hetero-oligomers. ESAT-6 showed a small, but measurable amount of self-
143 association, while CFP-10 showed no self-association. The dissociation constant (K_D) of the

144 ESAT-6/CFP-10 heterodimer has not hitherto been directly measured, but Renshaw et al.
145 estimated an upper bound of 10nM (Renshaw et al., 2002). We performed a detailed
146 measurement of the ESAT-6/CFP-10 association and measured a K_D of 220 pM, indicating
147 exceptionally tight binding (Fig 3C). ESAT-6 self-association resulted in reduced overall binding
148 to the sensor and displayed a rapid on rate, but also a rapid off rate (Fig 3D). The curve shape is
149 suggestive of something other than traditional 1:1 binding, but for comparison purposes we
150 calculated an apparent K_D of approximately 1.5 μM, weaker than that of the ESAT-6/CFP-10
151 association.

152 The pH of the Mtb-containing compartment typically ranges from 4.5 in IFN-γ activated
153 macrophages to 6.2 in non-activated macrophages (MacMicking et al., 2003; Vandal et al., 2008).
154 Because Mtb can exists in an acidified compartment, we tested whether ESAT-6 binding changes
155 under low pH conditions. Surprisingly, ESAT-6 displayed robust self-association at pH 4.5 (Fig
156 3E), resulting in several-fold more mass attaching to the sensor than even the ESAT-6/CFP-10
157 association at neutral pH. The apparent K_D for this interaction was slightly weaker than ESAT-6
158 self-association at neutral pH, but the total amount of binding was 20-30-fold greater, suggesting
159 that low pH conditions trigger ESAT-6 to assemble into larger complexes. Further, there have
160 been conflicting reports on whether ESAT-6 and CFP-10 dissociate from each other at low pH (de
161 Jonge et al., 2007; De Leon et al., 2012; Lightbody et al., 2008). Our results support the stable
162 interaction of ESAT-6 and CFP-10 at low-pH (Fig 3F), which exhibits an extremely tight apparent
163 K_D of 0.4 pM at pH 4.5: however, this is likely due to the multivalent ESAT-6 self-association
164 occurring in this condition (Fig 3G). To determine the precise pH at which ESAT-6 self-association
165 becomes dominant, we performed BLI experiments at half pH units from 4.5 to 6.5 (Fig 3H). We
166 found that 5.0 was the most basic pH at which increased self-association occurred.

167 ## Formation of large ESAT-6 complexes at pH 4.5

168 The response from pH 4.5 ESAT-6 biosensors appeared to increase past the typical
169 association time of our BLI assay. Because of this, we extended the binding time to 20 minutes
170 (Fig 4A), but the increasing self-association of ESAT-6 continued at roughly the same rate
171 throughout. To explore the possibility of complex formation and to determine the timeframe over
172 which this occurs, we next performed turbidity assays in which 50 μM of either ESAT-6 or CFP-
173 10 were brought to pH 4.5 or 7.5 and A_{350} was measured by plate reader for 1 hour (Fig 4B). We
174 observed an increase in turbidity at pH 4.5 but not 7.5 which was greater for ESAT-6 than CFP-
175 10, in line with previous findings (De Leon et al., 2012).

176 The BLI experiments we have shown thus far using the streptavidin-coated biosensors
177 (Fig 3A), have utilized ESAT-6 which had been biotinylated using succinimide chemistry
178 (ChromaLINK, Vector labs) allowing for precise quantification of incorporated biotin. Using 3 molar
179 equivalents of labeling reagent, we obtained ESAT-6 with an average of 0.99 biotins/protein.
180 However, succinimide chemistry can label any primary amine including the N-terminus and lysine
181 residues. ESAT-6 normally contains 3 lysines, and the pMRLB.7 construct contains 1 additional
182 lysine for a total of 4 (Fig 4C). Because it is unknown which region of the protein may be involved
183 in self-association, we generated an additional ESAT-6 construct capable of C-terminal site-
184 directed biotinylation via sortase-mediated transpeptidation via an LPETG motif (Fig 4C)
185 (Guimaraes et al., 2013; Popp et al., 2009). We performed additional BLI experiments using the
186 ESAT-6-LPETG construct and were able to verify similar behavior at neutral and acidic pH (Fig
187 4D-F).

188 ## Stoichiometry of ESAT-6 complexes

189 We next visualized the large ESAT-6 complexes by fluorescence microscopy in order to
190 get an idea of their scale. We mixed unmodified ESAT-6 with ESAT-6-LPETG-Biotin at a 10:1 ratio
191 and incubated on a poly-lysine coated coverslip, fixed, then stained with streptavidin-AF488 to

192 visualize ESAT-6 complexes. Fluorescence microscopy shows the development of individual
193 strands with the appearance of a heavily kinked thread or beads on a string (Fig 5A). These
194 structures were not present at neutral pH or when 6M guanidine was added to acidified ESAT-6.

195 To analyze the stoichiometry of these complexes, we next performed SEC coupled with
196 multi-angle light scattering (MALS), which can measure the molecular weight of complexes as
197 they elute from the SEC column. At pH 7.5, we observed a single peak with an approximate
198 molecular weight of 21 kDa, which most likely corresponds to an ESAT-6 homodimer (Fig 5B).
199 We did not observe the presence of any monomeric ESAT-6, indicating that it likely self-pairs in
200 the absence of CFP-10. This agrees with our BLI results from (Fig 3C). At pH 4.5, we were
201 surprised to see a single, well-defined peak at 46 kDa, most likely corresponding to a tetramer
202 (Fig 5C). No measurable monomer, dimer, or higher molecular weight complexes were observed.
203 While it is not surprising that the high molecular weight complexes observed (Fig 5A) were unable
204 to traverse the SEC column intact, it was unexpected that tetramers would be the only species
205 observed.

206 To address the question of the likely conformation of the homodimer and tetramer, we
207 performed modeling experiments using docking followed by molecular dynamics (MD) simulations
208 to estimate the most stable conformations. We started with a homology model based on
209 previously reported structures of the ESAT-6/CFP-10 heterodimer (PDB: 3FAV, 4J11, 4J7K, 4J10
210 and 4J7J) (Fan et al., 2015; Poulsen et al., 2014). To estimate the structure of the ESAT-6
211 monomer, we then performed a molecular dynamics simulation to observe the structural stability
212 of the protein's conformation. We observed that the energy-minimized structure of monomeric
213 ESAT-6 strongly resembles its conformation in the heterodimer. The helix-turn-helix structure
214 exhibits strong amphipathic nature, with both helices aligning to form a hydrophobic face flanked
215 by charged residues (Fig 5D).

We next modeled an ESAT-6 homodimer, starting again with a homology model based on the heterodimer followed by a molecular dynamics simulation. The homodimer model showed head-to-tail alignment of the ESAT-6 monomers associating via their hydrophobic faces and stabilized on either side by salt bridges (Fig 5E). This homodimer model represents a likely conformation of the species observed in the pH 7.5 SEC-MALS experiment (Fig 5B).

To model the tetrameric species observed in the acidic SEC-MALS experiment (Fig 5C), we performed docking of ESAT-6 homodimers and then a molecular dynamics simulation of the lowest energy conformation observed in docking. We observed the dimers interacting in a head-to-tail orientation via their hydrophilic faces, supported by salt bridges (Fig 5F). In the tetramer model, some of the charged residues, such as Lys_{67}, which had previously supported the dimer interface, switched orientations to support the tetramer interface.

For each of these models, the molecular dynamics informs us about the proteins' conformational stability. The root mean square fluctuation (RMSF) quantifies the amount of movement along the peptide backbone for each residue, with lower values equating to more stability. We performed molecular dynamics experiments for ESAT-6 in monomer, dimer, and tetramer forms in order to evaluate the stability of each species (Fig 5G). In general, the α-helices of ESAT-6 are stable, while the C- and N-termini are highly flexible. However, in the monomeric form, the residues between 20 and 50 exhibit increased flexibility at pH 7.5. At pH 4.5, the monomeric form exhibits increased flexibility along a majority of the backbone. At both pH values, dimerization (and tetramerization) result in greater overall stability. At pH 7.5, the average RMSF of the monomer is 2.51, which reduces to 2.33 for the dimer due to the reduced flexibility between residues 20 and 50. The tetramer is only marginally more stable, at 2.27. At pH 4.5, the difference between each state is even more pronounced, with an RMSF of 2.74, 2.04, and 1.94 for the monomer, dimer, and tetramer, respectively.

240 ## Generation and characterization of an ESAT-6 specific nanobody

241 We generated an ESAT-6-specific alpaca-derived nanobody using our previously reported
242 phage display method (Alfadhli et al., 2021; Bachran et al., 2017; Weinstein et al., 2022). E11rv
243 was generated by immunization and panning against pMRLB.7 ESAT-6. Following initial isolation,
244 we performed biochemical characterization, starting with ELISA experiments to determine the
245 EC_{50} of E11rv, which was found to be 1.26 μM (Fig 6A). We then determined the binding kinetics
246 via BLI, which we performed on both pMRLB.7 ESAT6 as well as our ESAT-6-LPETG construct
247 to ensure that the tag was not essential for binding (Fig 6B-C). E11rv bound similarly to ESAT-6
248 and ESAT-6-LPETG with K_Ds of 331 nM and 376 nM, respectively.

249 To determine the binding site, we performed hydrogen deuterium exchange experiments
250 with ESAT-6 (Harris et al., 2023; Masson et al., 2019; Rathinaswamy et al., 2021). This involves
251 incubating either apo or E11rv-bound ESAT-6 in D_20 buffer for different lengths of time. The
252 deuterium will exchange with acidic protons in the protein at different rates depending on the
253 solvent exposure, giving insights into which areas of the protein are more tightly folded, or
254 shielded by protein-protein interactions with a nanobody (Fig 6D-F). Digestion followed by MS
255 allows quantification of the extent of deuteration along the peptide backbone and concomitant
256 binding site estimation. For E11rv, we observed decreased deuteration compared to apo around
257 positions 50-65 (on the C-terminal helix, near the loop), and to a lesser extent positions 98-110
258 (within the tag). The region between these segments, from residues 66-94, displayed an increase
259 in solvent exposure, as did residues 14-28, on the opposing helix directly across from 66-94. A
260 likely explanation for this pattern is that E11rv binds around residues 50-65, and that this somehow
261 destabilizes the C-terminal portion of the helix or separates the helices enough to allow more
262 solvent exposure between helices. It is unclear how the small region within the tag might be
263 involved, but Fig 6B suggests that the positioning of the tag has little impact on binding, and this
264 region is predicted to be largely unstructured.

265 ### E11rv inhibits Mtb replication in macrophages.

266 We next performed functional testing of E11rv using two complementary approaches for
267 measuring the growth and viability of internalized Mtb in macrophages. The first of these
268 experiments used a live/dead reporter strain of Mtb based on H37Rv which constitutively
269 expresses mCherry and dox inducible expression of GFP, which has been shown to correlate with
270 CFU count (Martin et al., 2012). We infected THP-1 cells with live/dead reporter Mtb pre-incubated
271 with E11rv or an isotype control, then allowed the infection to proceed for 3 days before inducing
272 GFP with doxycycline for 24 hours. After fixing and staining for actin to reveal the location of cells,
273 we performed fluorescence microscopy on the infected cells. We then used CellProfiler to identify
274 all Mtb within images by their red fluorescence and calculated the GFP/RFP ratio for each
275 identified bacterium (Stirling et al., 2021). In this experiment, we found that E11rv led to a
276 statistically significant reduction in Mtb viability (Fig 7A,B).

277 The second functional assay we performed was based on continuous growth
278 measurement of luminescent LuxABCDE-expressing Mtb (Andreu et al., 2010; Leddy et al.,
279 2023). We prepared stable THP-1 cell lines with cytoplasmic expression of E11rv or an isotype
280 nanobody. We then infected the nanobody-expressing THP-1 cells with luminescent Mtb and
281 monitored their growth continuously via plate reader for 5 days, and we found that E11rv reduced
282 the growth rate substantially (Fig 7C). Over the full 5 days, the isotype-expressing cells allowed
283 the Mtb to grow to 6-fold over its starting value while the E11rv-expressing cells reduced this to
284 just under 3-fold.

285 ## Discussion

286 This study has several key findings. Firstly, ESAT-6 undergoes rapid self-association into
287 large complexes at pH levels below 5.0, and this may be preceded by formation of stable
288 tetramers. Second, in the absence of CFP-10, ESAT-6 exists as a homodimer at neutral pH. Third,

289 our nanobody, E11rv, binds to ESAT-6 and can inhibit the growth of Mtb inside cells when treated
290 externally or via cytoplasmic expression.

291 The issue of incomplete information about the amino acid sequence of one of the most
292 widely used ESAT-6 constructs is surprising, but none of the data we have generated suggested
293 a practical difference with differently tagged constructs. Previous studies have found major
294 differences in function between recombinant ESAT-6 in general when compared with “native”
295 ESAT-6 purified from Mtb cultures, which are typically purified using much harsher techniques
296 than recombinant protein due to the lack of affinity tags. One attractive theory for the observed
297 difference between recombinant and native ESAT-6 which is gaining traction is N-terminal
298 acetylation being required for ESAT-6 function, but this has not yet been proven in Mtb infection
299 (Aguilera et al., 2020; Collars et al., 2023; Mba Medie et al., 2014; Okkels et al., 2004). The most
300 commonly given reason for the importance of N-acetylation is that acetylated ESAT-6 is more
301 easily released from CFP-10 under acidic conditions. Our results suggest that purified ESAT-6
302 exists in a dimerized state in the absence of CFP-10, but our Native-PAGE (Fig 2A) and SEC (Fig
303 1C) demonstrate that purified ESAT-6 has no trouble interacting with CFP-10 to form a 1:1
304 complex. It is unclear whether the observed 1:1 complex is an ESAT-6/CFP-10 heterodimer
305 formed by exchange between ESAT-6 and CFP-10 homodimers, or if we are instead observing
306 formation of a tetramer composed of one each ESAT-6 and CFP-10 homodimers. Further, our low
307 pH BLI results (Fig 3F) suggest that self-associated ESAT-6 has no difficulty interacting with CFP-
308 10.

309 Our modeling and SEC-MALS data suggest that ESAT-6 can interact with itself using both
310 of its faces, one of which is hydrophobic, and one of which is hydrophilic; and both of which are
311 supported by salt bridges formed by charged residues at either edge. This implies that ESAT-6
312 may still be able to self-associate within membranes via its hydrophilic face. This agrees with the
313 putative requirement for compartment acidification in order to drive membrane damage, as our

314 data suggests that low pH is required for self-association at this interface, but likely does not affect
315 the hydrophobic interface, which must then require a different mechanism for dissociation and
316 membrane insertion. Some have suggested that other mycobacterial factors may help facilitate
317 the membrane insertion of ESAT-6, such as phthiocerol dimycocerosates (Augenstreich et al.,
318 2020, 2017).

319 Modeling approaches have also been used previously to propose an organized ESAT-6
320 pore structure using similar logic, but these have yet to be supported by physical evidence (Karki
321 et al., 2020; Refai et al., 2015). However, there is precedent for ESAT-6-like WXG proteins to form
322 organized membrane channels, with a recent study demonstrating a pentameric EsxE/EsxF
323 structure capable of membrane insertion and toxin trafficking (Tak et al., 2021). Critically, EsxE
324 does not dissociate from EsxF in order to insert into the membrane. Such structures have yet to
325 be observed with ESAT-6/CFP-10, but this may just be a matter of finding the appropriate
326 conditions and reagents.

327 Finding molecular tools to interrogate the function of Mtb virulence factors remains a
328 challenge due to the complexity of accessing Mtb in its native environment within the phagosome.
329 The nanobody described here presents a novel way of targeting the bacteria *in situ*, which we
330 demonstrated by modulating its growth using intracellularly expressed E11rv. Because E11rv
331 showed functional effects both when added in the media and when expressed inside the cell
332 cytoplasm, it suggests a significant amount of communication between Mtb inside the phagosome
333 and other compartments of the cell. This is consistent with the findings of many other studies
334 which show numerous putative activities for ESAT-6 such as induction of apoptosis (Behura et
335 al., 2019; Choi et al., 2010; Lim et al., 2016; Yang et al., 2015), inhibition of interferon-γ production
336 (Kumar et al., 2012; Peng et al., 2011), inhibition of autophagy (Dong et al., 2016; Romagnoli et
337 al., 2012; Yabaji et al., 2020), inhibition of antigen presentation (Sreejit et al., 2014), induction of
338 type I interferon (Jang et al., 2018; Lienard et al., 2020), and a more recent study showing an

339 ESX-1-dependent mechanism for incorporation of Mtb antigens into MHC-I presentation via
340 cytosolic antigen processing (Leddy et al., 2023). Most of these functions rely on ESAT-6 getting
341 into the cytoplasm, and this may occur via disruptions in the phagosomal membrane to establish
342 two-way communication between compartments, or by complete phagosomal escape of Mtb into
343 the cytoplasm.

344 Author Contributions

345 Timothy A Bates: Conceptualization, Methodology, Validation, Formal Analysis, Investigation,
346 Data Curation, Writing – Original Draft, Writing – Review & Editing, Visualization, Supervision,
347 Project Administration, Funding acquisition.

348 Mila Trank-Greene: Conceptualization, Methodology, Validation, Investigation, Data Curation,
349 Writing – Review & Editing, Visualization.

350 Xammy Nguyenla: Methodology, Investigation, Writing – Review & Editing.

351 Aidan Anastas: Methodology, Investigation, Writing – Review & Editing.

352 Ilaria R Merutka: Methodology, Investigation, Writing – Review & Editing.

353 Shandee D Dixon: Methodology, Investigation, Writing – Review & Editing.

354 Anthony Shumate: Methodology, Investigation, Writing – Review & Editing.

355 Matthew AH Parson: Methodology, Software, Validation, Formal Analysis, Investigation, Data
356 Curation, Visualization.

357 Eric Barklis: Conceptualization, Methodology, Writing – Review & Editing.

358 John E Burke: Conceptualization, Formal Analysis, Resources, Supervision, Project
359 Administration, Funding acquisition.

Ujwal Shinde: Conceptualization, Methodology, Software, Validation, Formal Analysis, Investigation, Data Curation, Writing – Review & Editing, Visualization.

Hidde L Ploegh: Conceptualization, Resources, Writing – Review & Editing, Funding acquisition.

Fikadu G Tafesse: Conceptualization, Methodology, Validation, Formal Analysis, Resources, Writing – Original Draft, Writing – Review & Editing, Supervision, Project Administration, Funding acquisition.

Acknowledgements

This study was supported by the Bill & Melinda Gates foundation grant OPP1179922 (to FGT), NIH R01AI141549 (to FGT), Silver Family Innovation Fund (to FGT), NHLBI training grant 5T32HL083808 (to TAB). BLI data were generated on an Octet Red 384, which is made available and supported by the OHSU Biophysics Shared Resources Core and equipment grant number S10OD023413. Mass spectrometry experiments were performed with support from Dr. Larry L. David and the OHSU Proteomics Shared Resource core.

Competing interests

HLP serves as an advisor to and owns stock in Cerberus Therapeutics. HLP serves as a consultant to Johnson and Johnson, Immatics Therapeutics, Cue Biopharma, Revela Therapeutics, and Tiba Bio. JEB reports personal fees from Scorpion Therapeutics, Reactive therapeutics and Olema Oncology; and research grants from Novartis. All other authors declare that they have no competing interests.

379 # Methods

380 ## Plasmids and primers

381 ### Plasmids

Name	Description	Source
pMRLB.7	ESAT-6 expression vector	BEI Resources, NR-50170
pMRLB.46	CFP-10 expression vector	BEI Resources, NR-13297
pMRLB.7-LPETG	ESAT-6-LPETG expression vector	This study
pHEN	Nanobody expression vector	(Hoogenboom et al., 1991)
pInducer20	Lentiviral expression vector	(Meerbrey et al., 2011)

382 ### Primers

Name	Sequence
T7 (sequencing primer)	TAATACGACTCACTATAGGG
ESAT-6-Fw	CCGGAAACCGGCGGCATCAAGCTTATCGATACCGTCGACCTC
ESAT-6-Rv	GCCGCCGGTTTCCGGGAGCTCTGCGAACATCCCAGTG

383 ## Cloning ESAT-6-LPETG

384 ESAT-6-LPETG was generated by in vivo assembly (IVA) as described previously (García-
385 Nafría et al., 2016). PCR was performed on pMRLB.7 using ESAT-6-Fw and ESAT-6-Rv primers
386 using Q5 polymerase with the following recipe and cycle design. Reactions were treated with DpnI
387 for 15 minutes at 37°C. 2 µL of reaction mixture was added directly to 50 µL of chemically
388 competent DH5-α cells, incubated on ice for 30 minutes, heat shocked at 42 for 30 seconds, then
389 immediately added to 200 µL of SOC, after which it was recovered for 30 minutes at 37°C and
390 plated on Luria Bertani (LB)-ampicillin (amp) agar plates, and incubated overnight at 37°C. Clones
391 were sequence confirmed before further use.

392 ## Expression and purification of ESAT-6 and CFP-10

393 pMRLB.7, pMRLB.46, and pMRLB.7-LPETG were transformed into *Escherichia coli* BL21
394 Rosetta rare codon competent cells. 25 mL Luria Bertani (LB) starter cultures were grown
395 overnight at 37°C with shaking with 100 ug/mL ampicillin to stationary phase. Each starter culture
396 was used to inoculate 1L of LB, which was then grown at 37°C until reaching an OD_{600} of 0.8, at
397 which point it was induced with 0.1 mM IPTG for 4 hours at 37°C. Bacteria was pelleted by
398 centrifugation at 6,000×g for 10 minutes, then frozen at –80°C. Pellets were thawed and
399 resuspended in 25 mL of 10 mM Tris HCl, 300 mM NaCl, 10% glycerol, 10 mM Imidazole, 1 ug/mL
400 DNase and RNase, 0.5 mg/ml Lysozyme, 10 mM DTT, and 1 tablet/100 mL Sigma fast EDTA free
401 protease inhibitor (Lysis buffer) for 20 minutes. Lysates were sonicated on ice for 30 seconds on
402 and 30 seconds off for a total of 5 minutes. Crude lysates were then clarified by centrifugated at
403 20,000×g for 20 minutes. Supernatant was decanted and spun again similarly. Ni-NTA beads were
404 washed with 10 mM Tris HCl, 300 mM NaCl, 10 % glycerol (wash buffer). Lysate was applied to
405 0.5 mL of Ni-NTA beads per liter of bacteria and rocked for 1 hour at 4°C then poured over a 25
406 mL chromatography column. The column was then washed with 10 column volumes of wash
407 buffer plus 10 mM Imidazole, and then eluted in 10 mL wash buffer plus 250 mM Imidazole.
408 Protein containing fractions (assessed by SDS-PAGE) were pooled and imidazole was then buffer
409 exchanged and concentrated with 3 kDa MWCO centrifugal concentrator. Protein concentration
410 was assessed by A_{280}, correction for extinction coefficient. Purity was determined by SDS-PAGE,
411 and α-His_6 western blot.

412 ## Western blot

413 15% SDS-PAGE gels were run with 1 µg of protein, and transferred to a PVDF membrane
414 (0.2 µm pore size) for 1 hour at 4°C, using a wet transfer tank (Trans-blot, Bio Rad). The
415 membrane was rinsed with deionized (DI) water and blocked with 2% non-fat dry milk (Lab
416 Scientific #978-907-4243) in tris buffered saline with 0.1% Tween-20 (TBST) for 30 minutes at

417 room temperature (RT). Blots were stained with 1:10,000 α-His_6-HRP (Invitrogen, MA1-80218) in
418 blocking buffer overnight at 4°C. Blots were then washed with PBST three times for 5 minutes
419 each. Signal was developed using SuperSignal Western Pico PLUS (Thermo Scientific)
420 chemiluminescent substrate according to the manufacturer's instructions and visualized on an
421 ImageQuant LAS 4000.

422 Size exclusion chromatography (SEC)

423 SEC was performed on a HiLoad 16/600 Superdex 75 pg (Cytiva) column on an
424 ÄKTApurifier FPLC (GE) system. Sterile filtered and degassed 10 mM Tris HCl, 300 mM NaCl, 10
425 % glycerol, pH 7.8 was used as a mobile phase and was run at 0.8 mL/min at 4°C. Data was
426 collected with Unicorn 5.31 (GE).

427 Native polyacrylamide gel electrophoresis (PAGE)

428 15% polyacrylamide gels were cast with 3.5 mL 30% acrylamide:0.8% bis-acrylamide,
429 1.7mL of 1.5 M Tris HCl buffer, 70 µL of 10% ammonium persulfate, and 7 µL of TEMED per gel.
430 To analyze the dimerization of CFP10 and ESAT6, 25 µM stocks of each protein were made,
431 mixed in varying ratios, and incubated for 60 minutes at 4 C. Non-denaturing loading buffer was
432 added and reactions were loaded then run at 4°C overnight at 50 V in Tris-Glycine buffer without
433 SDS (National Diagnostics) and then Coomassie stained.

434 Hemolysis

435 Bacterial hemolysis

436 Hemolysis experiments were performed as described previously (Conrad et al., 2017).
437 Sheep blood (HemoStat labs, SBC100) was washed with PBS by centrifugation at 3200×g for 5
438 minutes and resuspended to a final concentration of 1% (v/v) red blood cells (RBC) in PBS.
439 Bacterial cultures, Mm, Mtb, MtbΔRD1 were grown in Middlebrook 7H9 with OADC to an OD_{600}
440 between 0.3 and 1.0. Cultures were washed with PBS by centrifugation at 500×g for 5 minutes

441 and resuspended in PBS. The equivalent of 3 mL of culture at OD_{600} 1.0 was resuspended in 100
442 µL of PBS and combined with 100 µL of 1% RBCs. Centrifuged samples at 3200×g for 5 minutes,
443 then incubated the pelleted samples at 37°C for Mtb and MtbΔRD1, or 33°C for Mm for 2 hours.
444 Samples were then resuspended by pipette and spun again similarly. The absorbance at 405 nm
445 was measured for each sample using a plate reader, as well as for samples without bacteria and
446 samples with 0.1% Triton-X100. Percent hemolysis was calculated as (A_{405}Sample – A_{405}PBS) ÷
447 (A_{405}Triton – A_{405}PBS) × 100.

448 Protein hemolysis

449 For measurement of protein hemolysis, RBCs were resuspended to 1% (v/v) in McIlvaine
450 buffer of pH 4.5, 5.5, 6.5, 7.5, and 8.5 prepared as previously described (McIlvaine, 1921). 100
451 µL of 1 mg/mL ESAT-6 was combined with 100 µL of 1% RBC solution and incubated at RT for 1
452 hour. Samples were then spun at 3200×g for 5 minutes and the A_{405} supernatants were measured
453 by plate reader. PBS and Triton samples were prepared similarly to bacterial hemolysis, and %
454 hemolysis was calculated using the same formula.

455 Biolayer interferometry (BLI)

456 BLI was performed using an Octet Red384 machine (ForteBio). Octet Streptavidin
457 Biosensors (Sartorius, #18-5019) were used for all experiments. Biotinylated proteins were
458 prepared using the succinimide (ESAT-6, CFP-10, RBD) or sortase (ESAT-6-LPETG, E11rv, VHH
459 52) method. Recombinant SARS-Cov-2 spike RBD was used as a loading control for ESAT-6 and
460 CFP-10 experiments, while VHH 52 against influenza was used as a loading control for E11rv
461 experiments. For all experiments, Biosensors were soaked for 20 minutes in DI water, blocked for
462 30 seconds in 10mM Citrate, 100mM NaCl, 3mM EDTA, 0.1% BSA, 0.005% Tween-20 (running
463 buffer) which was adjusted to match the pH of the test condition (4.5, 5.0, 5.5, 6.0, or 7.5).
464 Biotinylated protein was then loaded onto the biosensors until approximately 1 nm of binding
465 response was observed. Excess protein was washed off with three cycles of 15 seconds in 10

466 mM glycine pH 1.7 then 15 seconds in running buffer. Washing was followed by a 30 second
467 baseline step in running buffer, an association step with test analyte diluted in running buffer, then
468 dissociation step in plain running buffer. When multiple conditions were tested, the lowest
469 concentration was tested first, and 3 wash cycles were performed between conditions. Loading
470 control biosensors followed the same protocol with identical sample concentrations. Data was
471 collected with Octet Data Acquisition 10.0.0.87 (ForteBio), and data was analyzed with Octet Data
472 Analysis HT 10.0.0.48 (ForteBio). Background subtraction was performed using loading control
473 biosensors, data was aligned to the average of the baseline step, and smoothed by Savitzky-
474 Golay filtering. All data were fit to a 1:1 model using the "full (assoc and dissoc) setting" using the
475 entire step length. Reported kinetic binding constants (K_D, K_{ON}, and K_{OFF}) values were calculated
476 by taking the geometric mean of binding constants calculated for individual conditions and
477 replicates. Conditions were excluded from the average when the Data Analysis HT software was
478 unable to calculate all constants for a given condition due to insufficient signal. The only conditions
479 excluded using this criterion were ESAT-6 pH 7.5 self-association at 0.316 nM, and E11rv
480 association with ESAT-6 and ESAT-6-LPETG at 0.33 and 0.1 μM.

481 ## Turbidity assay

482 ESAT-6 was buffer exchanged into PBS using a Zeba spin column (ThermoFisher) and
483 diluted to a concentration of 50 μM. 30 μL of ESAT-6 was added to each well in a 384 well plate.
484 To each well, 2 μL of either PBS or Citrate buffer was added. Citrate buffer contained 50mM citric
485 acid and 100 mM NaCl, and was adjusted for pH such that mixing 5mL buffer with 45mL PBS
486 resulted in a solution with pH 4.5. Plates were immediately added to a plate reader following pH
487 adjustment and A_{350} was read every 2 minutes for a total of 60 minutes with 10 seconds of shaking
488 between each read. Turbidity was calculated as A_{350}Sample – A_{350}PBS.

489 ## Biotinylation

490 ### Succinimide biotinylation

491 Recombinant ESAT-6, CFP-10, and RBD (lacking an LPETG tag) were biotinylated using
492 the ChromaLINK biotinylation kit (Vector labs). Manufacturer's instructions were used. 3 molar
493 equivalents of biotinylation reagent yielded a labeling level of 0.99 biotins/protein calculated using
494 the E1% method in the manufacturer's labeling calculator. Proteins were buffer exchanged into
495 PBS by passing through a PBS-equilibrated Zeba desalting column (ThermoFisher, 89882).
496 Protein aliquots were snap frozen in liquid nitrogen and stored at -80°C until use.

497 ### Sortase biotinylation

498 ESAT-6-LPETG and LPETG-tagged nanobodies were C-terminally biotinylated using
499 sortase as previously described (Guimaraes et al., 2013; Popp et al., 2009). Briefly, 20 µL of 20
500 mg/mL sortase enzyme, 20 µL of 10 mM GGG-Biotin peptide, and 200 µL of 1mg/mL LPETG-
501 labeled protein. This mixture was incubated at 4°C overnight, then added to 50 uL of packed,
502 PBS-washed Ni-NTA beads to remove the His-tagged sortase enzyme and any unreacted protein
503 for 2 hours at 4°C. The resulting supernatant was buffer exchanged into PBS by passing through
504 a PBS-equilibrated Zeba desalting column (ThermoFisher, 89882). Protein aliquots were snap
505 frozen in liquid nitrogen and stored at -80°C until use.

506 ## Protein microscopy

507 Coverslips were coated in poly-L-Lysine at 4°C overnight, washed once with PBS, then
508 dried before use. A 9:1 molar ratio of ESAT-6:ESAT-6-LPETG-Biotin (final concentration 0.24
509 mg/mL) was prepared prior to addition of 10× citrate buffer prepared similarly to the turbidity
510 assay. The guanidine-containing sample used a protein concentration of 0.7 mg/mL and included
511 a final concentration of 2M guanidine. The treated protein mixtures were incubated at RT for 30
512 minutes. Five 2µL drops were added to each coverslip and incubated at RT for 30 minutes.

513 Coverslips were fixed by addition of 4% formaldehyde in PBS for 30 minutes at RT, washed three
514 times with PBS, blocked in 2.5% BSA in PBS for 30 minutes at RT, washed 3 times with PBS,
515 stained with 1:10,000 (in PBS) streptavidin-AF488 (Jacskon Immuno, 016-540-084), and finally
516 washed 3 times with PBS. Coverslips were mounted onto microscope slides with Prolong Gold
517 antifade (ThermoFisher, P10144). Images were captured on a Zeiss LSM 980 with Airyscan2
518 using a 63× oil objective and processed with Zeiss Blue Airyscan joint deconvolution.

519 Size exclusion chromatography multi-angle light scattering (SEC-MALS)

520 SEC-MALS was performed on an AKTApure FPLC (Cytiva) with a DAWN MALS detector
521 (Wyatt). 100 µg of ESAT-6 was buffer exchanged with a Zeba spin column immediately prior to
522 each experiment and injected onto a Superdex 75 increase 10/300 column at a flow rate of 0.5
523 mL/min at 4°C. The mobile phase was 10 mM Citrate, 300 mM NaCl, pH 4.5 or pH 7.5. Buffers
524 were sterile filtered to 0.1 µm and degassed prior to use. Data analysis was performed using
525 ASTRA 8.1.2.1 (Wyatt).

526 Modeling

527 Homology Modeling

528 The ESAT6 and CFP10 protein sequences were modeled via the Homology Modeling
529 protocol in YASARA version 22.09.24. Sidechain optimization occurred through the FoldX plugin,
530 with an energy minimization using AMBER14 force-field. X-ray structures with specified PDB IDs:
531 3FAV-A, 4J11-B, 4J7K-B, 4J10-A and 4J7J-B (PDB ID-Chain) served as templates for full-length
532 modeling of both proteins, with alternative models considered if alignments were unclear. For
533 CFP10, about 66% aligned with the template, and specific residues (MAEMKTDAAT and
534 RADEEQQQAL) were predicted using loop modeling. Similarly, around 69% of ESAT6 aligned,
535 with residues (STEGNVTGMF and MTEQQW) modeled as described earlier. After side-chain
536 building and optimization, new model components underwent combined steepest descent and

537 simulated annealing minimization. YASARA then integrated the best model parts to create a high-
538 accuracy hybrid for each protein. Structures, dihedrals, and 1D to 3D packing were inspected for
539 optimal monomer models. Dimer models were based on orientations from the 3FAV template,
540 while tetrameric structures were predicted using dimer models as templates via the M-Zdock
541 server.

542 Molecular Dynamic Simulations

543 The protonation status of amino acid residues and subsequent alteration of side-chain
544 interactions and the domain structure can be influenced by the pH, impacting the stability,
545 dynamics, and/or interactions of CFP10, ESAT6, and their heterodimers. As such, these were
546 examined at both pH 4.5 and 7.4 through molecular dynamics simulations. These simulations,
547 performed under the NPT ensemble with periodic boundary conditions, provided a sampling of
548 the conformational space available to the various oligomeric forms of ESAT6 and CFP10. The
549 domains were subjected to MD simulations for a period of 50 ns and snapshots were taken at 250
550 ps intervals for later examination. Each simulation process was run twice with distinct random
551 seeds to confirm the reliability of the simulations. The RMSF of each simulation was plotted as
552 displayed in the Figure.

553 Nanobody discovery

554 Nanobody discovery was performed as previously described (Weinstein et al., 2022).
555 Briefly, Alpacas were immunized with recombinant ESAT-6 protein and immune serum was
556 collected. Peripheral blood mononuclear cells (PBMC) were isolated and RNA was extracted with
557 an RNeasy mini kit (Qiagen 74104), which was then converted to cDNA using Superscript III
558 (Invitrogen 18080051). VHH genes were amplified using gene specific primers for long- and shot-
559 hinge heavy-chain-only antibodies (Maass et al., 2007). Amplified VHH genes were cloned into a
560 phagemid vector based on pCANTAB-5E and transformed into competent TG1 *E. coli*. The
561 bacterial library was infected with helper phage to generate a phage library and purified by PEG

562 precipitation (Frei and Lai, 2016). The phage library which was panned against recombinant
563 ESAT-6 to enrich strong binders. Panning consisted of incubating the purified phage library in
564 antigen-coated tubes and then eluting with pH 2.2 glycine. Eluted phage were neutralized with
565 1M Tris pH 9.1, and transferred to log-phase ER2738 *E. coli*, to produce the enriched library,
566 which was plated on agar. Individual ER2738 clones were selected and screened by ELISA to
567 quantify affinity. E11rv was selected for further testing based on its performance in the screening
568 ELISA, and was cloned into the pHEN periplasmic expression plasmid.

569 Nanobody purification

570 Nanobodies were purified by periplasmic purification. pHEN plasmid containing each
571 nanobody was transformed into *E. coli* WK6 competent cells. 20 mL starter cultures were grown
572 overnight at 37 C with shaking in Terrific Broth (2% tryptone, 1% yeast extract, 90mM phosphate)
573 with 100 ug/mL ampicillin to stationary phase. Starter cultures were used to begin 1L Terrific Broth
574 cultures to be grown at 37C. When cultures reached OD600 of approximately 0.6 OD, they were
575 induced with 1 mM IPTG overnight at 30 C. Bacteria was pelleted at 4,000 xg for 10 minutes and
576 resuspended in 40 mLs of lysis buffer (200 mM HEPES, 0.65 mM EDTA, 0.5 M sucrose, at cold
577 pH 8), then incubated at 4C for 1-2 hrs. Add 40 mLs of ice cold water and incubate for 2 hrs,
578 rotating, to lyse periplasm by osmotic shock. Periplasmic fraction was isolated by centrifuging
579 lysate at 8,000 xg for 15 minutes, twice. VHH E11 was purified with Ni-NTA chromatography.
580 Purified E11 was then buffer exchanged and concentrated with 3kDa cutoff centrifuge filters
581 (Millipore), then aliquoted and frozen for future use.

582 Enzyme linked immunosorbent assay (ELISA)

583 ELISA experiments were performed as described previously (Weinstein et al., 2022).
584 MaxiSorp plates (Invitrogen 442404) were coated with ESAT-6 at 5 µg/mL in PBS overnight at
585 4°C. Plates were blocked in 2% BSA, 2% Polyvinylpyrrolidone (PVP), 0.1% Tween-20 in PBS
586 (blocking buffer) for 30 minutes at RT. Dilutions of E11rv or isotype control VHH 52 were made in

587 blocking buffer and added to plates for 1 hour at RT with shaking. Plates were washed with PBST
588 3 times for 5 minutes each and biotinylated anti-VHH antibody (Jackson Immuno 128-065-232)
589 at 1:10,000 in blocking buffer was added for 1 hour at RT with shaking. Plates were washed again
590 and incubated with 1:10,000 streptavidin-HRP (Jackson Immuno 016-030-084) in blocking buffer
591 for 1 hour at RT. Plates were washed again and incubated with 50 µL of ODP (ThermoFisher
592 34006), prepared according to the manufacturer's instructions, for 15 minutes before stopping
593 with 50 µL of 2N H_2SO_4. A_{492} was measured using a CLARIOstar PLUS (BMG) plate reader. Raw
594 data was background subtracted with wells lacking nanobody and normalized by dividing by the
595 highest binding well, then fit to a 4PL sigmoid curve in Prism 10.0.0 (Graphpad) to determine the
596 EC_{50}.

597 Hydrogen-deuterium exchange (HDX)

598 HDX-MS sample preparation

599 HDX reactions comparing ESAT6 Apo to E11rv-bound were carried out in 30 µl reaction
600 volumes containing 15 pmol of ESAT6. A protein mastermix was created for both reaction
601 conditions (500 nM ESAT6, 1 µM E11rv or equivalent volume of E11rv buffer). The exchange
602 reactions were initiated by the addition of 25 µL of D_2O buffer (20 mM HEPES pH 7.5, 100 mM
603 NaCl) to 5 µL of protein mastermix (final D_2O concentration of 78.6% [v/v]). Reactions proceeded
604 for 0.3s (3s on ice), 3s, 30s, 300s, and 3000s at 20°C before being quenched with ice cold acidic
605 quench buffer, resulting in a final concentration of 0.6M guanidine HCl and 0.9% formic acid post
606 quench. All conditions and timepoints were created and run in independent triplicate. Samples
607 were flash frozen immediately after quenching and stored at -80°C until injected onto the ultra-
608 performance liquid chromatography (UPLC) system for proteolytic cleavage, peptide separation,
609 and injection onto a QTOF for mass analysis, described below.

610 ## Protein digestion and MS/MS data collection

611 Protein samples were rapidly thawed and injected onto an integrated fluidics system
612 containing a HDx-3 PAL liquid handling robot and climate-controlled (2°C) chromatography
613 system (LEAP Technologies), a Dionex Ultimate 3000 UHPLC system, as well as an Impact HD
614 QTOF Mass spectrometer (Bruker). The full details of the automated LC system are described in
615 (Stariha et al., 2021). The samples were run over one immobilized pepsin column (Waters;
616 Enzymate Protein Pepsin Column, 300Å, 5µm, 2.1 mm X 30 mm) at 200 µL/min for 3 minutes at
617 2°C. The resulting peptides were collected and desalted on a C18 trap column (Acquity UPLC
618 BEH C18 1.7mm column (2.1 x 5 mm); Waters 186003975). The trap was subsequently eluted in
619 line with an ACQUITY 1.7 µm particle, 100 × 1 mm^2 C18 UPLC column (Waters), using a gradient
620 of 3-35% B (Buffer A 0.1% formic acid; Buffer B 100% acetonitrile) over 11 minutes immediately
621 followed by a gradient of 35-80% over 5 minutes. Mass spectrometry experiments acquired over
622 a mass range from 150 to 2200 m/z using an electrospray ionization source operated at a
623 temperature of 200°C and a spray voltage of 4.5 kV.

624 ## Peptide identification

625 Peptides were identified from a non-deuterated sample of ESAT6 using data-dependent
626 acquisition following tandem MS/MS experiments (0.5 s precursor scan from 150-2000 m/z;
627 twelve 0.25 s fragment scans from 150-2000 m/z). MS/MS datasets were analysed using PEAKS7
628 (PEAKS), and peptide identification was carried out by using a false discovery-based approach,
629 with a threshold set to 0.1% using a database of purified proteins and known contaminants. The
630 search parameters were set with a precursor tolerance of 20 ppm, fragment mass error 0.02 Da,
631 charge states from 1-8, leading to a selection criterion of peptides that had a -10logP score of
632 16.2.

633 ## Mass Analysis of Peptide Centroids and Measurement of Deuterium Incorporation

634 HD-Examiner Software (Sierra Analytics) was used to automatically calculate the level of
635 deuterium incorporation into each peptide. All peptides were manually inspected for correct
636 charge state, correct retention time, appropriate selection of isotopic distribution, etc. Deuteration
637 levels were calculated using the centroid of the experimental isotope clusters. Results are
638 presented as relative levels of deuterium incorporation and the only control for back exchange
639 was the level of deuterium present in the buffer (78.6%). Differences in exchange in a peptide
640 were considered significant if they met all three of the following criteria: ≥4.5% change in
641 exchange, ≥0.45 Da difference in exchange, and a p value <0.01 using a two tailed student t-test.
642 Samples were only compared within a single experiment and were never compared to
643 experiments completed at a different time with a different final D_2O level. The data analysis
644 statistics for all HDX-MS experiments are in **Supplemental Table 1** according to the guidelines
645 of (Masson et al., 2019). The mass spectrometry proteomics data have been deposited to the
646 ProteomeXchange Consortium via the PRIDE partner repository (Perez-Riverol et al., 2022).

647 ## Imaging-based Mtb viability assay

648 Live/Dead H37rv Mtb constitutively express mCherry and have Tet^{ON} inducible GFP
649 expression. THP-1 cells were seeded at 40,000 cells/well in glass bottom, black-walled 96 well
650 tissue culture plates and treated with 100 μM Phorbol-12-myristate-13-acetate (PMA) for 24 hours
651 prior to infection. Endotoxin free E11rv and unrelated isotype nanobodies were prepared to 1
652 mg/mL and sterile filtered prior to use. THP-1 cells were infected at an MOI of 1 with Live/Dead
653 Mtb was pre-incubated for 30 minutes with 100 μg/mL of nanobody. Infected plates were
654 incubated for 3 days in tissue culture conditions. Doxycyline was added to a final concentration
655 of 1 μg/mL and incubated for 24 hours. Plates were fixed with 5% formaldehyde in PBS for 1 hour
656 at RT in accordance with OHSU biosafety procedures before removing plates from the BSL3.
657 Plates were then washed with PBS and stained with Phalloidin-AF405 at 1:40 from 6.6 μM stock

658 for 1 hour. Wells were imaged with a Keyence (BZX-710) using a 20× S Plan Fluor ELWD lens.
659 49 images were captured for each well using the same exposure settings for each experiment.
660 Images were analyzed with CellProfiler 4.2.5 (Stirling et al., 2021). Images with obvious defects
661 such as large dust particles were excluded from the analysis. Mean GFP / Mean RFP was
662 calculated for each identified TB particle and the average GFP/RFP value was tabulated for each
663 image. Images were plotted as individual points in Prism (Graphpad) as described in the statistics
664 section.

665 Continuous luminescence viability assay

666 THP-1 cells were transduced with lentivirus to express nanobody-GFP fusion constructs
667 for E11rv and VHH 52 under a Tet^{ON} promoter (pInducer20 plasmid). The lentiviruses were
668 generated as described previously (Niekamp et al., 2021). THP-1 cells were transduced and
669 selected with 600 µg/mL of G418 for 3 weeks, then maintained with 300 µg/mL G418 in every
670 other passage. For each experiment opaque white 96-well plates were seeded with 30,000
671 cells/well along with a matched clear plate, both including 100 nM PMA. Cells were incubated
672 with PMA for 24 hours before inducing with 1 µg/mL doxycycline for another 24 hours. Cell health
673 and nanobody expression was verified by microscopy of the clear plate. The opaque plate was
674 infected with bioluminescent pLux Mtb, which expresses the full luxABCDE cassette, at an MOI
675 of 1. The plate was sealed with a Beathe-Easy plate seal (Research Products International
676 248738) and put into a climate-controlled CLARIOstart plate reader for continuous luminescence
677 reading for 120 hours.

678 Statistics

679 Statistical analysis was performed in Prism 10.0.0 (Graphpad). In Figure 2B, two-tailed
680 one sample t-tests were performed with a significance cutoff of 0.05 against a hypothetical value
681 of 0. In figure 7B, a two-tailed unpaired t test was performed with a significance cutoff of 0.05. For
682 all plots, * = 0.05, ** = 0.01, *** = 0.001, **** = 0.0001.

683

684

685

686 # Figures

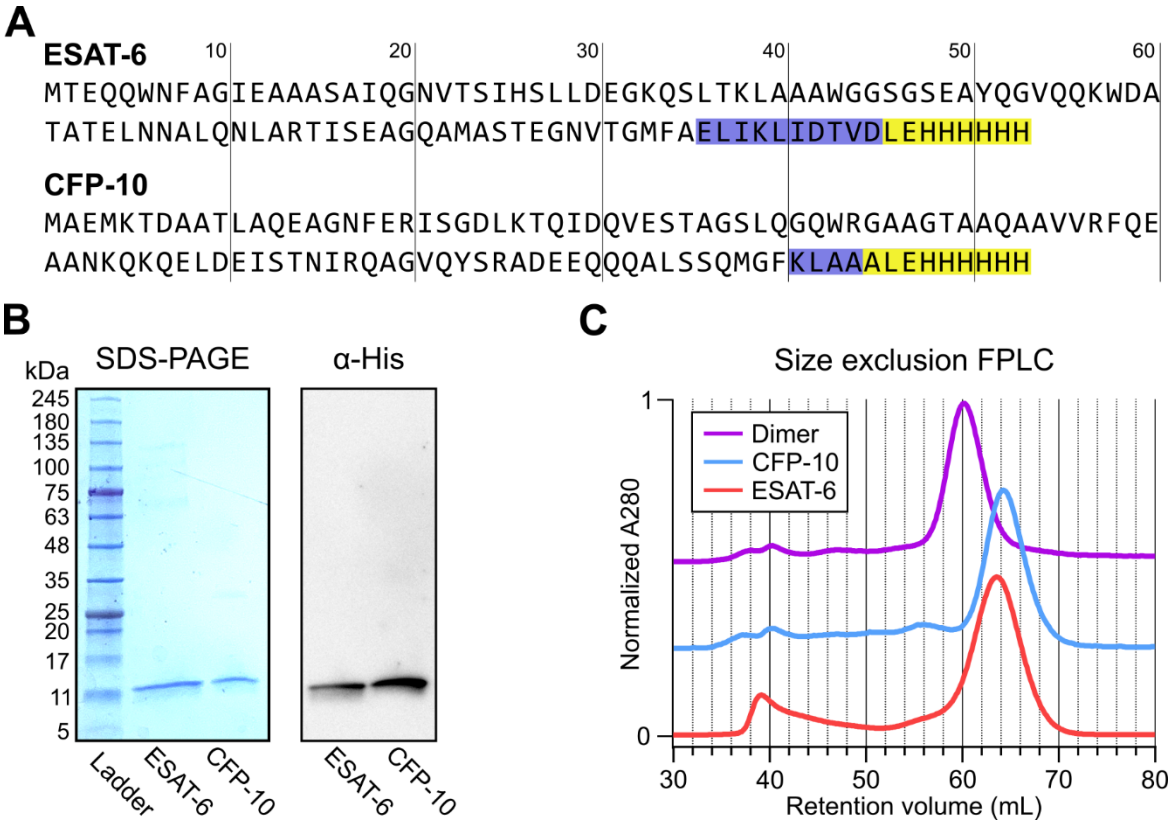

687

688 Figure 1: Expression of recombinant ESAT-6 and CFP-10. (A) amino acid sequences derived
689 from plasmid sequencing of pMRLB.7 (ESAT-6) and pMRLB.46 (CFP-10) plasmids available from
690 BEI Resources. The yellow highlights indicate the expected FALE-Histidine tag amino acid
691 sequence while the blue highlights indicate unexpected additional amino acids. (B) SDS-PAGE
692 gel of purified ESAT-6 and CFP-10 with a paired anti-His_6 western blot. (C) Size exclusion
693 chromatography traces showing the retention volumes of purified ESAT-6, CFP-10 and an
694 equimolar mixture of both (Dimer).

695

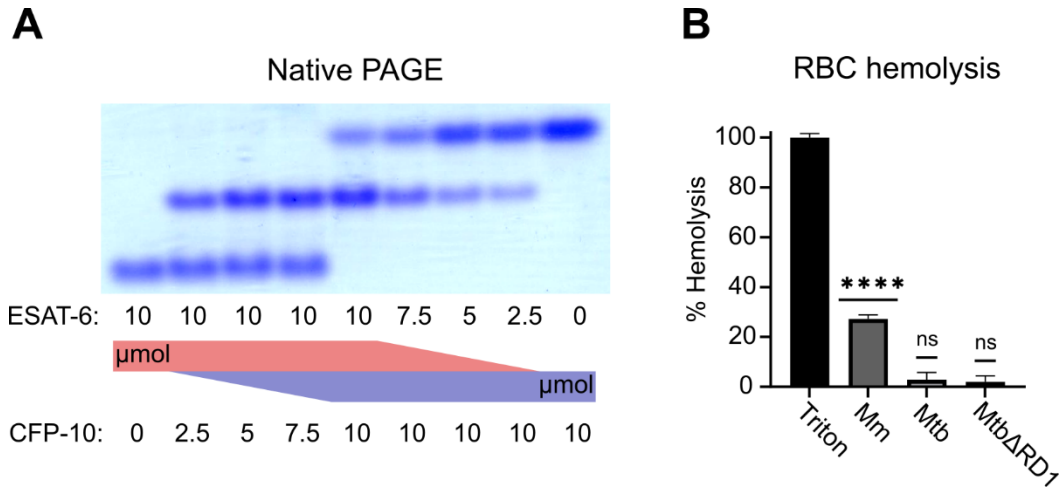

696

697 Figure 2: functional testing of ESAT-6 and CFP-10. (A) Native-PAGE analysis of ESAT-6 and
698 CFP-10 showing 1:1 complex formation at neutral pH. The displayed gel is representative of 3
699 replicates. (B) Contact-dependent red blood cell (RBC) hemolysis by whole bacteria, either
700 *Mycobacterium marinum* (Mm), *Mycobacterium tuberculosis* (Mtb), or Mtb with the region of
701 difference 1 deletion, incapable of producing ESAT-6 or CFP-10 (MtbΔRD1). Data in B represents
702 6 replicates. Statistical significance was determined using a one sample t test against a theoretical
703 mean of 0. * = 0.05, ** = 0.01, *** = 0.001, **** = 0.0001.

704

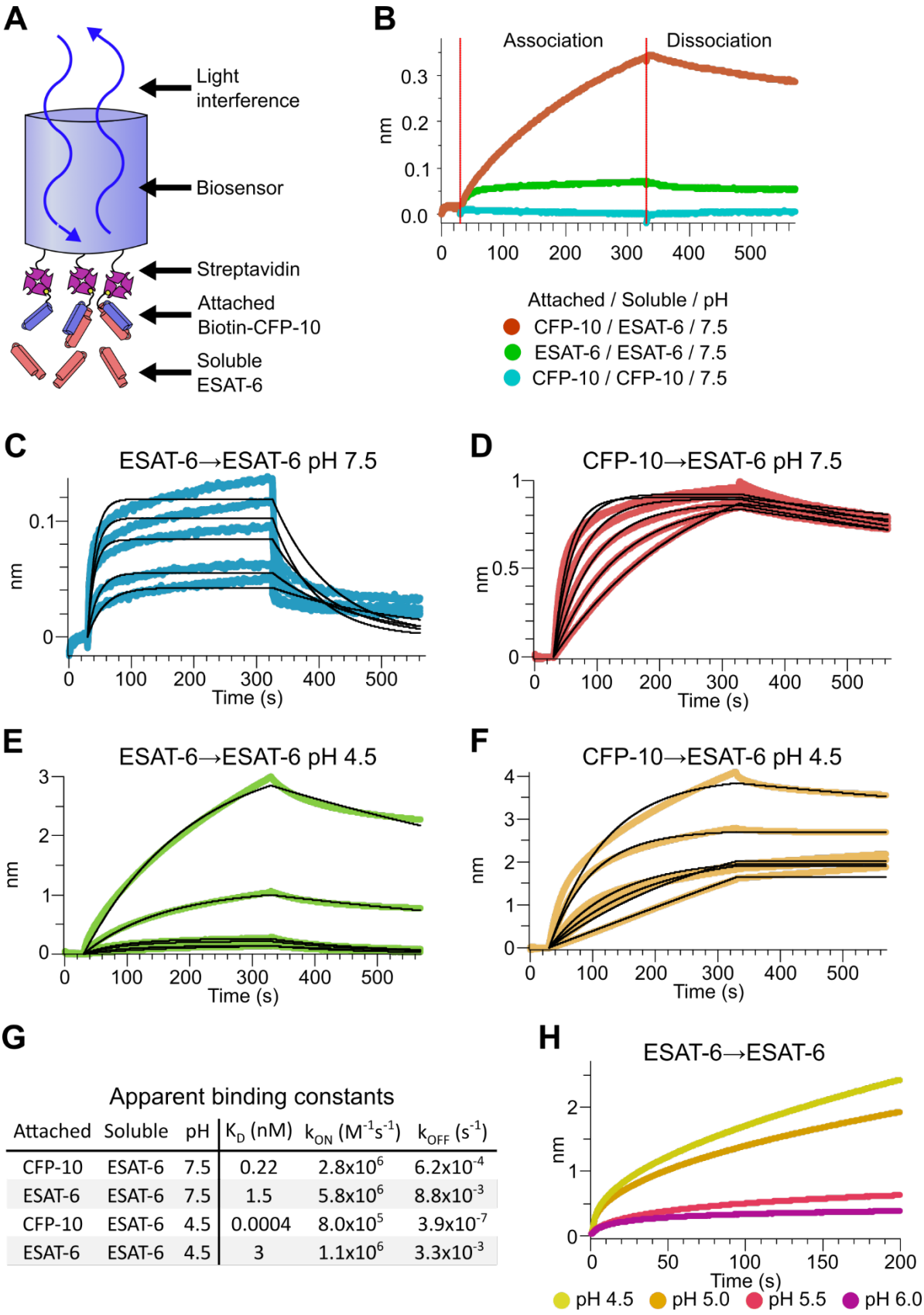

Apparent binding constants

Attached	Soluble	pH	K_D (nM)	k_{ON} ($M^{-1}s^{-1}$)	k_{OFF} (s^{-1})
CFP-10	ESAT-6	7.5	0.22	2.8×10^{6}	6.2×10^{-4}
ESAT-6	ESAT-6	7.5	1.5	5.8×10^{6}	8.8×10^{-3}
CFP-10	ESAT-6	4.5	0.0004	8.0×10^{5}	3.9×10^{-7}
ESAT-6	ESAT-6	4.5	3	1.1×10^{6}	3.3×10^{-3}

705

706 Figure 3: Binding kinetics of ESAT-6 and CFP-10 under neutral and acidic conditions. (A)
707 Biolayer interferometry (BLI) experimental design. Biotinylated ESAT-6 or CFP-10 are attached
708 to streptavidin coated biosensors, then dipped into solutions of free ESAT-6 or CFP-10. (B) BLI
709 experiment depicting ESAT-6 and CFP-10 association, ESAT-6 self-association, and CFP-10 self-
710 association at pH 7.5 with 50 μM. BLI experiment showing (C) ESAT-6 self-association at pH 7.5,
711 (D) CFP-10/ESAT-6 association at pH 7.5, (E) ESAT-6 self-association at pH 4.5, and (F) CFP-
712 10/ESAT-6 association at pH 4.5 Proteins in (C-F) were tested at 1, 3.16, 10, 31.6, and 100 μM.
713 (G) Table of apparent binding constants calculated with a 1:1 model for each indicated condition.
714 (H) BLI experiment testing ESAT-6 self-association at pH 4.5, 5.0, 5.5, and 6.0 with 100 μM
715 protein.

716

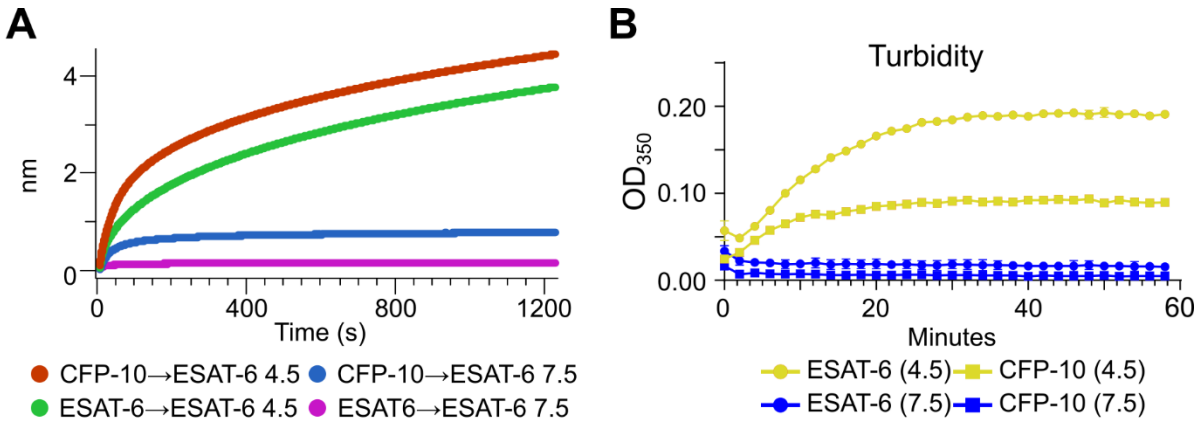

C

ESAT-6-Lysine-Biotin (~1 biotin incorporated per protein)

MTEQQWNFAGIEAAASAIQGNVTSIHSLLDEGKQSLTKLAAAWGGSGSEAYQGVQQKWDA
TATELNNALQNLARTISEAGQAMASTEGNVTGMFAELIKLIDTVDLEHHHHHH

ESAT-6-LPETG (before sortase reaction)

MTEQQWNFAGIEAAASAIQGNVTSIHSLLDEGKQSLTKLAAAWGGSGSEAYQGVQQKWDA
TATELNNALQNLARTISEAGQAMASTEGNVTGMFAELPETGGIKLIDTVDLEHHHHHH

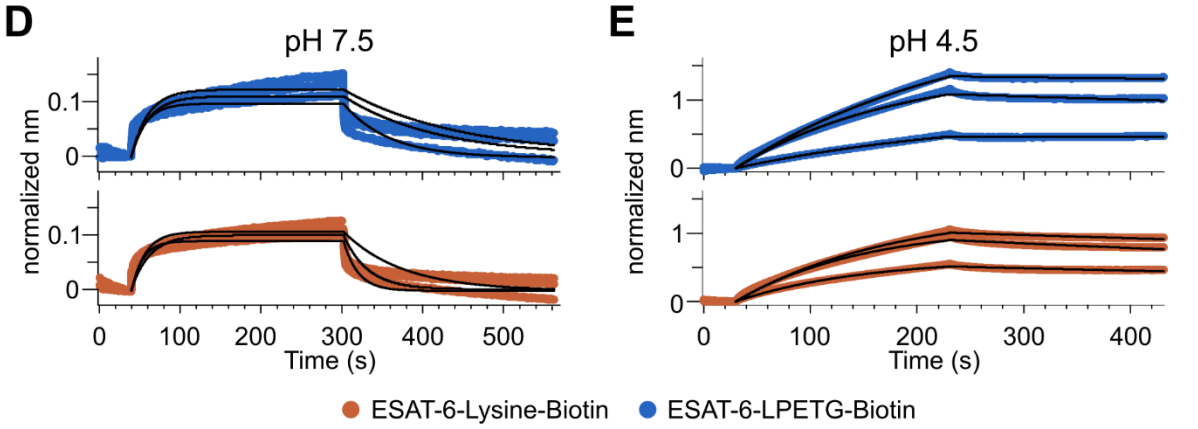

F

Apparent binding constants

Attached	Soluble	pH	K_D (nM)	k_{ON} ($M^{-1}s^{-1}$)	k_{OFF} (s^{-1})
ESAT-6-LPETG-Biotin	ESAT-6	7.5	12	$1.3x10^{6}$	$1.6x10^{-2}$
ESAT-6-Lysine-Biotin	ESAT-6	7.5	19	$1.6x10^{6}$	$3.1x10^{-2}$
ESAT-6-LPETG-Biotin	ESAT-6	4.5	0.8	$2.0x10^{5}$	$1.7x10^{-4}$
ESAT-6-Lysine-Biotin	ESAT-6	4.5	2.3	$2.9x10^{5}$	$6.8x10^{-4}$

Figure 4: Extensive self-association of ESAT-6. (A) BLI long-association experiment showing 50 μM ESAT-6 at pH 4.5 or 7.5 attaching to biosensors coated with either ESAT-6 or CFP-10. (B) Turbidity assay showing 50 μM ESAT-6 or 50 μM CFP-10 at pH 4.5 or 7.5 over time. Absorbance at 350nm read every 2 minutes. (C) Lysine-labeled Biotinylated ESAT-6 has an average of 1 biotin

722 per protein attached to the N-terminus or one of the orange highlighted lysine residues. The ESAT-
723 6-LPETG construct amino acid sequence is shown which includes and inserted LPETG motif, in
724 orange. Reaction with biotinylated poly-glycine via sortase-mediated transpeptidation results in
725 the teal highlighted residues being removed and replaced with a biotin molecule. BLI experiments
726 at (D) pH 7.5 and (E) pH 4.5 showing unmodified soluble ESAT-6 interacting with streptavidin
727 biosensor tips loaded with ESAT-6-Lysine-Biotin (red) or ESAT-6-LPETG-Biotin (blue). Curves
728 were normalized by dividing response values by the amount of protein added during the loading
729 step. (F) Summary of apparent kinetic binding constants in (D-E).

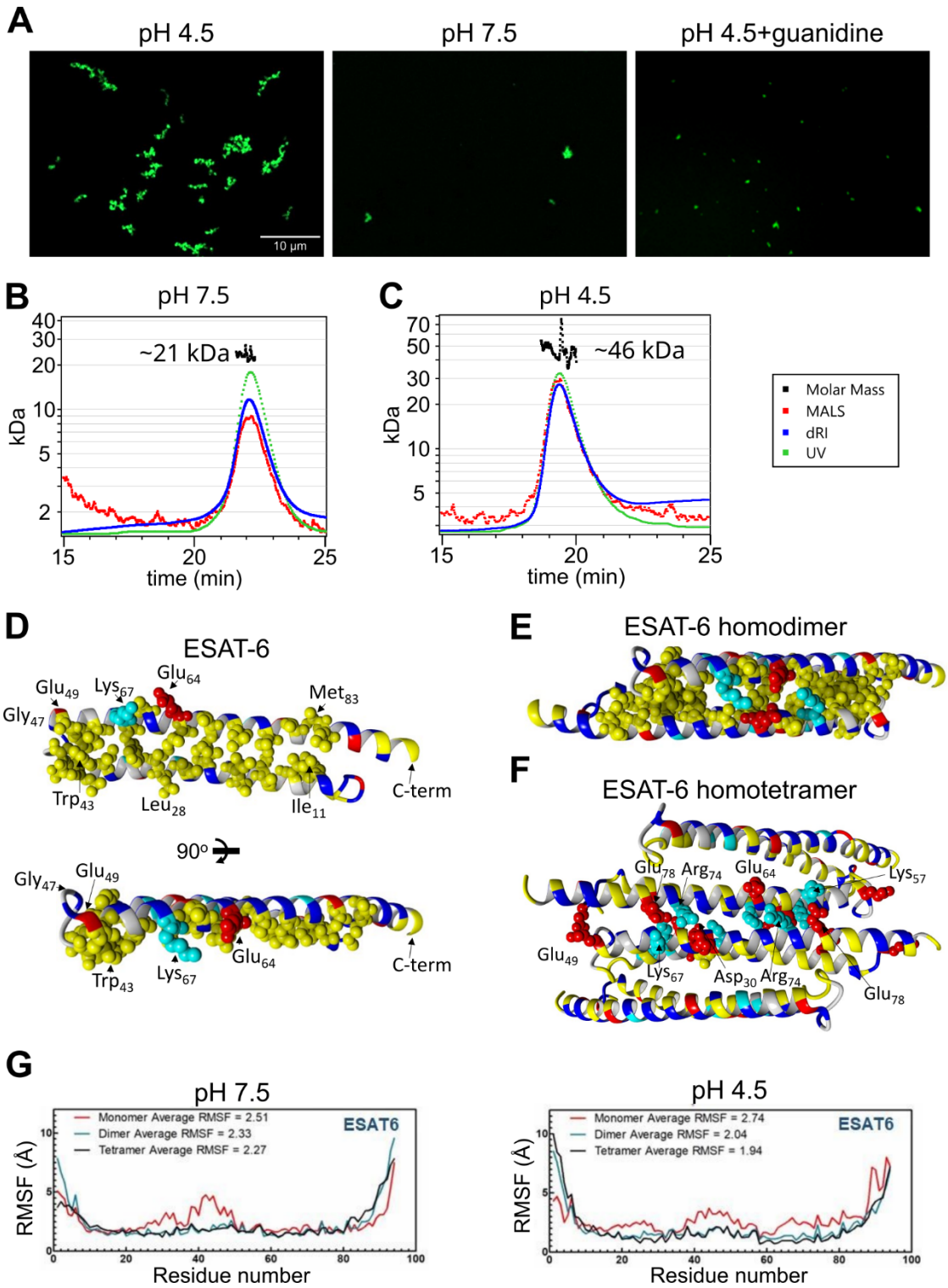

730

731 Figure 5: Stoichiometry of ESAT-6 self-interaction. (A) Fluorescence microscopy showing

732 fluorescently labeled ESAT-6 complexes under different conditions: pH 4.5, pH 7.5, and pH 4.5 +

733 6M guanidine. The images shown are representative of 3 replicates. Size exclusion

734 chromatography followed by multi-angle light scattering (SEC-MALS) traces showing UV
735 absorbance, refractive index (dRI), and MALS data along with calculated molar mass over the
736 peak at pH 7.5 (B), and pH 4.5 (C). Data in (B-C) is representative of 3 replicates. (D-F) Modeling
737 of ESAT-6 in monomeric (D), homodimeric (E), and homotetrameric form (F). Hydrophobic
738 residues are in yellow, polar residues are in blue, basic residues are in cyan, and acidic residues
739 are in red. Key side chain residues are shown as spheres. (G) Root mean square fluctuation
740 (RMSF) values are shown per residue for ESAT-6 monomer, dimer, and trimer at pH 7.5 and 4.5.

741

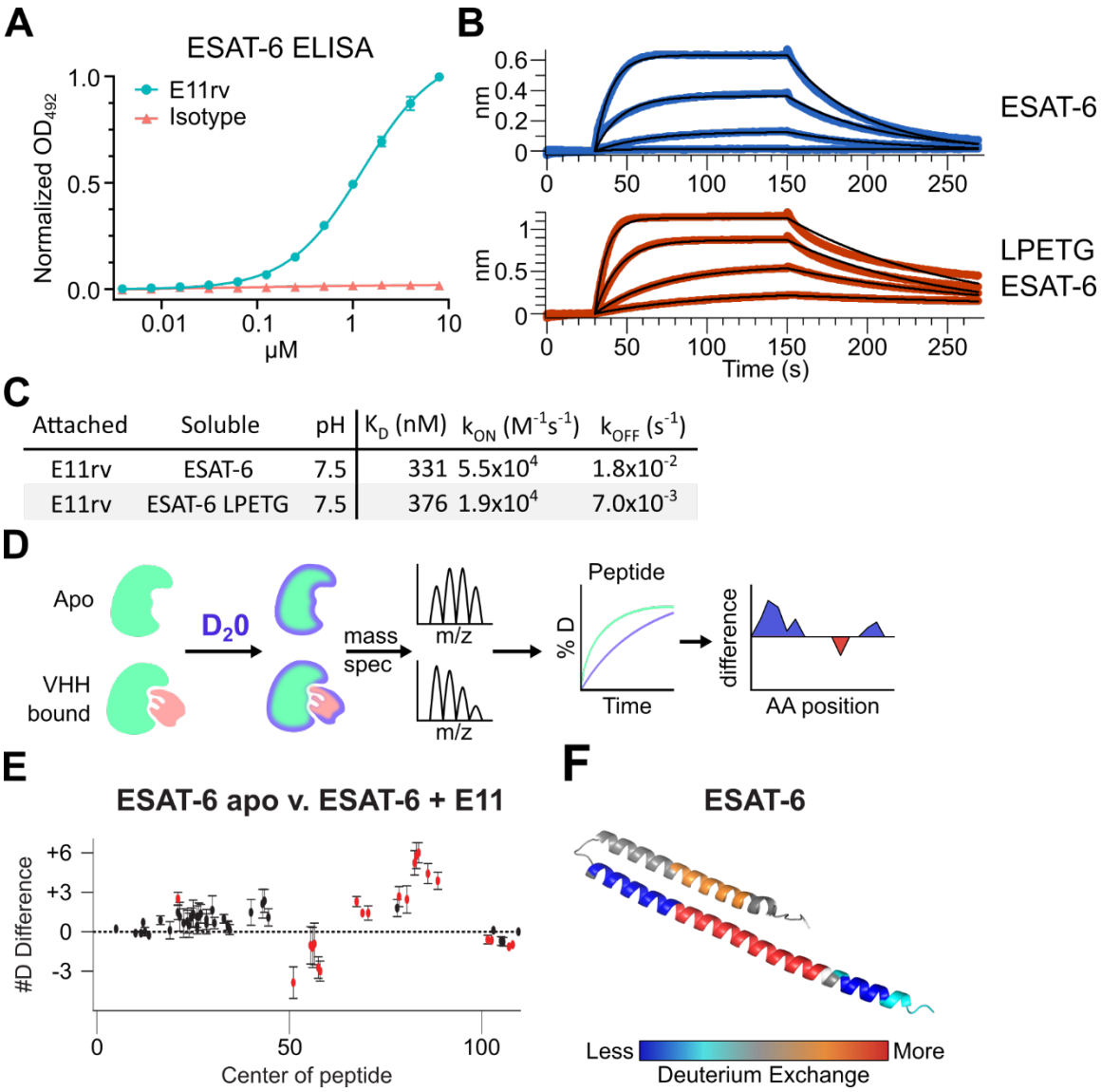

Figure 6: An ESAT-6-binding alpaca nanobody. (A) ELISA experiment on ESAT-6-coated plates showing nanobody E11rv and an irrelevant isotype control. E11rv displays an EC50 of 17.5 (95% CI 16.0-19.4) μg/mL. (B) BLI experiments with E11rv-coated biosensors tested against pMRLB.7 ESAT-6 (blue) or ESAT-6-LPETG (red) at 10, 3.3, 1, and 0.3 μM. (C) Summary of kinetic binding constants from (B). (D) schematic diagram of hydrogen-deuterium exchange (HDX) experiment showing apo ESAT-6 or E11rv-bound ESAT-6 incubated in D20, then subjected to digestion and mass spectrometry to measure the levels of deuterium incorporation at different times for different peptides, then mapping this to the protein sequence to identify areas with less

751 or greater deuterium exchange between the apo and bound conditions. (E) HDX data for ESAT-6
752 and E11rv showing reduced deuterium uptake around residue 50 and increased uptake around
753 residue 75. (F) HDX shifts mapped to the ESAT-6 structure (PDB: 3FAV).

754

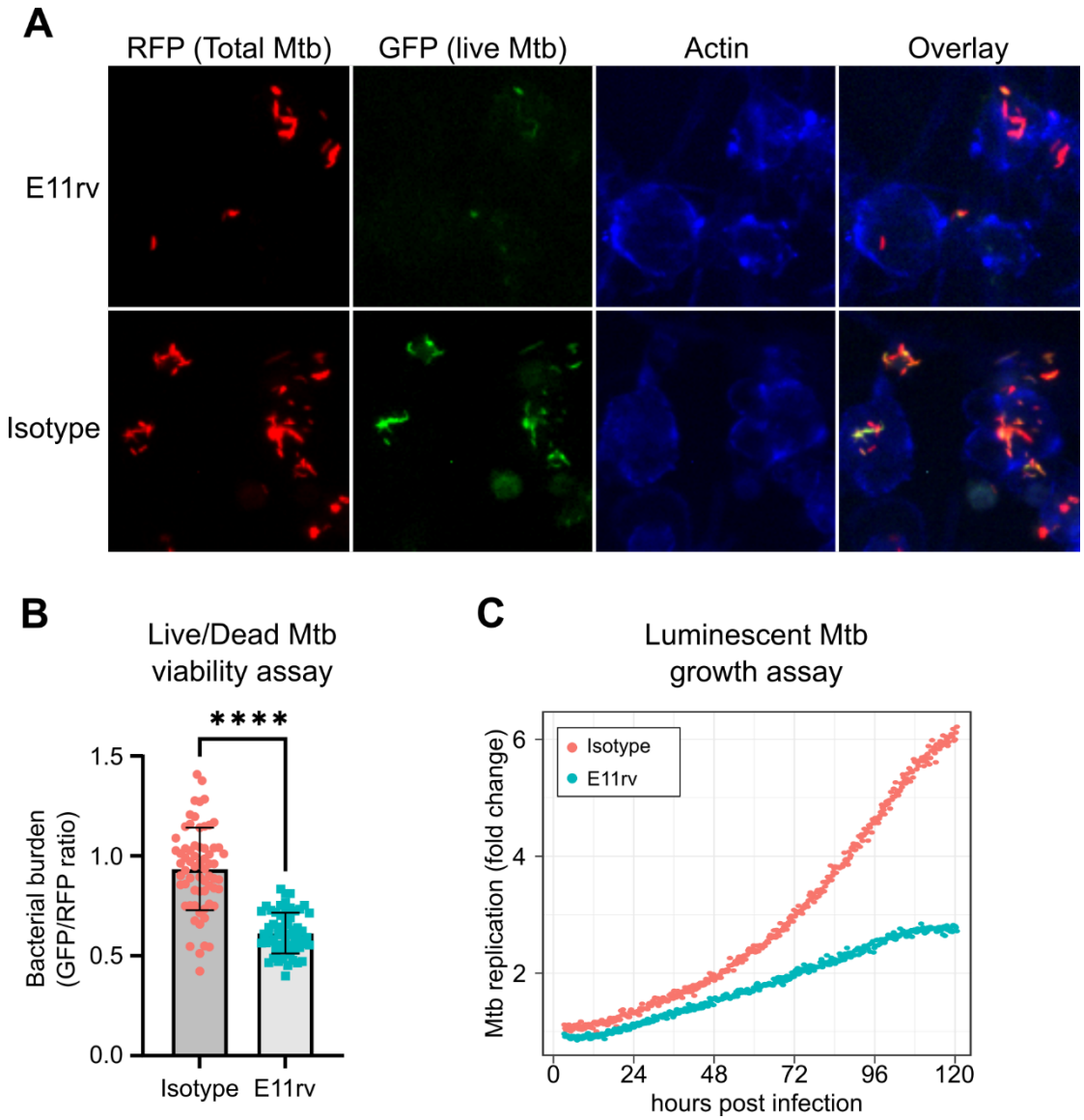

Figure 7: E11rv inhibits Mtb growth in cells. (A) representative fluorescence microscopy images for E11rv and isotype treated cultures. Results include data from 3 replicates. (B) Cellular assay testing the effect of infecting THP-1 cells with Live/Dead Mtb in the presence of E11rv for 3 days, treated with doxycycline for 24 hours to induce GFP expression by remaining metabolically active Mtb. The GFP/RFP ratio was calculated for each Mtb spot identified by fluorescence microscopy. Statistical significance was determined with a two-tailed unpaired t test. * = 0.05, ** = 0.01, *** = 0.001, **** = 0.0001. (C) Luminescence growth assay of stably transfected THP-1 cells expressing E11rv or isotype nanobody in their cytoplasm. Cells were infected with

764 luminescent Mtb and monitored by luminescence plate reader for 120 hours. Results are
765 representative of 6 replicates.

766

A

pMRLB.7 (ESAT-6)

```
                10        20        30        40        50        60
   1  CNNNNNNNCNNNNNANANTTTGTTTACTTTAAGAAGGAGATATACATATGACAGAGCAGC
  61  AGTGGAATTTCGCGGGTATCGAGGCCGCGGCAAGCGCAATCCAGGGAAATGTCACGTCCA
 121  TTCATTCCCTCCTTGACGAGGGGAAGCAGTCCCTGACCAAGCTCGCAGCGGCCTGGGGCG
 181  GTAGCGGTTCGGAGGCGTACCAGGGTGTCCAGCAAAAATGGGACGCCACGGCTACCGAGC
 241  TGAACAACGCGCTGCAGAACCTGGCGCGGACGATCAGCGAAGCCGGTCAGGCAATGGCTT
 301  CGACCGAAGGCAACGTCACTGGGATGTTCGCAGAGCTCATCAAGCTTATCGATACCGTCG
 361  ACCTCGAGCACCACCACCACCACCACTGAGATCCGGCTGCTAACAAAGCCCGAAAGGAAG
 421  CTGAGTTGGCTGCTGCCACCGCTGAGCAATAACTAGCATAACCCCTTGGGGCCTCTAAAC
 481  GGGTCTTGAGGGGTTTTTTGCTGAAAGGAGGAACTATATCCGGATTGGCGAATGGGACGC
 541  GCCCTGTAGCGGCGCATTAAGCGCGGCGGGTGTGGTGGTTACGCGCAGCGTGACCGCTAC
 601  ACTTGCCAGCGCCCTAGCGCCCGCTCCTTTCGCTTTCTTCCCTTCCTTTCTCGCCACGTT
 661  CGCCGGCTTTCCCCGTCAAGCTCTAAATCGGGGGCTCCCTTTAGGGTTCCGATTTAGTGC
 721  TTTACGGCACCTCGACCCCAAAAAACTTGATTANGGTGATGGTTCACGTAGTGGGCCATC
 781  GCCCTGATAGACGGTTTTTCGCCCTTTGACGTTGGAGTCCACGTTCTTTAATAGTGGACT
 841  CTTGTTCCAAACTGGNACAACACTCAACCCTATCTCGGTCTATTCTTTTGATTTATNANG
 901  NTTTTGCCGATTTCGGCCTATTGGNTAAAAATGAGCTGATTTAACAAAATTTAACGCGAA
 961  TTTANNNAATANTAACGCTTACATTTANNNGCACTTTTCGGGGAAATGTGCGNGACCCTN
1021  NTTGTTATTTTTCNAANACNTCANTATGNANCNCTCATGANANATANCNTGANAANGNTC
1081  ANAATNTNAAANNNNNNNATNANNATCANATTTCNNNNCNCCTATNCCNTTTNNNNGNNT
1141  TTNNNTNCNNNTTTNNNN
```

B

pMRLB.46 (CFP-10)

```
                10        20        30        40        50        60
   1  NNNNNNNNNNNNNNNNNNNNNNNNNTTTTGTTTAACTTTAAGAAGGAGATATACATATGGC
  61  AGAGATGAAGACCGATGCCGCTACCCTCGCGCAGGAGGCAGGTAATTTCGAGCGGATCTC
 121  CGGCGACCTGAAAACCCAGATCGACCAGGTGGAGTCGACGGCAGGTTCGTTGCAGGGCCA
 181  GTGGCGCGGCGCGGCGGGGACGGCCGCCCAGGCCGCGGTGGTGCGCTTCCAAGAAGCAGC
 241  CAATAAGCAGAAGCAGGAACTCGACGAGATCTCGACGAATATTCGTCAGGCCGGCGTCCA
 301  ATACTCGAGGGCCGACGAGGAGCAGCAGCAGGCGCTGTCCTCGCAAATGGGCTTCAAGCT
 361  TGCGGCCGCACTCGAGCACCACCACCACCACCACTGAGATCCGGCTGCTAACAAAGCCCG
 421  AAAGGAAGCTGAGTTGGCTGCTGCCACCGCTGAGCAATAACTAGCATAACCCCTTGGGGC
 481  CTCTAAACGGGTCTTGAGGGGTTTTTTGCTGAAAGGAGGAACTATATCCGGATTGGCGAA
 541  TGGGACGCGCCCTGTAGCGGCGCATTAAGCGCGGCGGGTGTGGTGGTTACGCGCAGCGTG
 601  ACCGCTACACTTGCCAGCGCCCTAGCGCCCGCTCCTTTCGCTTTCTTCCCTTCCTTTCTC
 661  GCCACGTTCGCCGGCTTTCCCCGTCAAGCTCTAAATCGGGGGCTCCCTTTAGGGTTCCGA
 721  TTTAGTGCTTTACGGCACCTCGACCCCAAAAAACTTGATTAGGGTGATGGTTCACGTAGT
 781  GGGNCATCGCCCTGATAGACGGNTTTTCGCCCTTTGACGTTGGAGTCCACGTTCTTTAAT
 841  AGTGGACTCTTGTTCCAANCTGGAACAACACTCAACCCTATCTCGGTCTATTCTTTTGAT
 901  TTATANGGATTTTGCCGATTTCGGCCTATTGGTTAAAAAATGAGCTGANTTAACNAAAAT
 961  TTAACGCGAATTTTNACNAAATATTAACGCTTNNAANTTANNNGGCACTTTTCGGGGAAN
1021  NGNNNNCGGAACCCCTATTTGGTNNTTTTTTCTAAATACATNCAANNNGNANCCGCTCNT
1081  NANANATAACCNNGANNNNGCTTCANAANNTTGAAAAGGAANANNNNNAGTATTCNANAN
1141  NTCNNGNNNCCCNNNNNNNN
```

767

768 Supplemental Figure S1: Sequencing of. (A) Sanger sequencing of pMRLB.7 with the ESAT-
769 6 open reading frame (ORF) highlighted grey. (B) Sanger sequencing of pMRLB.46 with the CFP-
770 10 ORF highlighted grey.

771

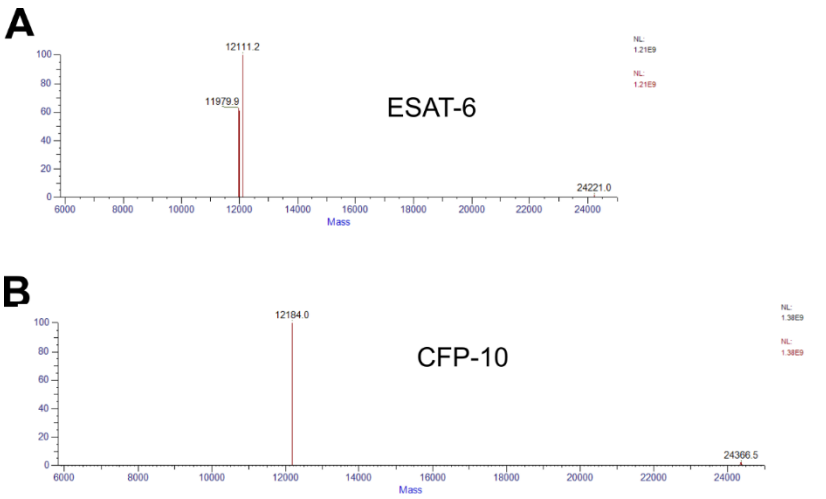

C

	Computed mass (Da)	Measured mass (Da)	Fractional abundance (%)
ESAT-6	12109.2	12111.2	62
ESAT-6ΔMet1	11978.0	11979.9	38
CFP-10	12313.4	ND	0
CFP-10ΔMet1	12182.2	12184.0	100

Supplemental Figure S2: Whole protein mass spectrometry (MS) of recombinant ESAT-6 and CFP-10. (A) Deconvoluted mass spectrum of recombinant ESAT-6 MS run. (B) Deconvoluted mass spectrum of recombinant CFP-10 MS run. (C) Computed mass of each protein compared with the measured masses. Fractional abundance combined the main peak with the harmonic artifact at twice the mass and gives an approximate relative proportion of each molecule in the sample. ESAT-6 is approximately 38% demethionylated while CFP-10 is fully demethionylated.

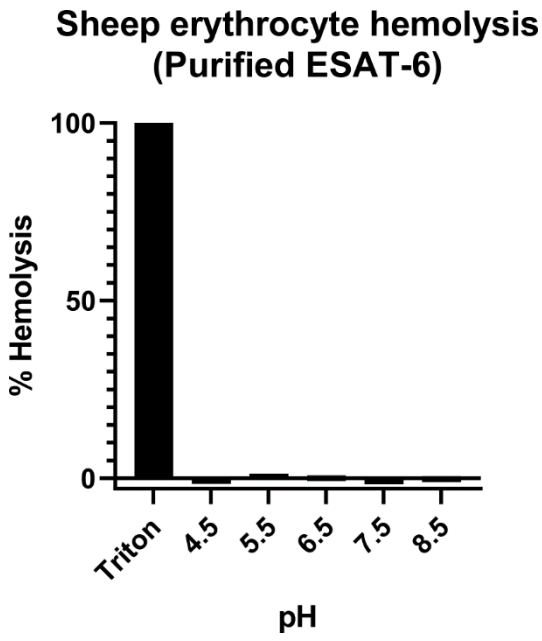

Supplemental Figure S3: Hemolysis by recombinant ESAT-6. (A) Sheep red blood cell hemolysis assay carried out with purified ESAT-6 in citrate buffer at various pH values. Percent hemolysis was calculated by subtracting buffer background and dividing by Triton-X100 detergent lysed samples.

789 # References Cited:

790 Aguilera, J., Karki, C.B., Li, L., Reyes, S.V., Estevao, I., Grajeda, B.I., Zhang, Q., Arico, C.D.,
791 Ouellet, H., Sun, J., 2020. Nα-Acetylation of the virulence factor EsxA is required for
792 mycobacterial cytosolic translocation and virulence. J. Biol. Chem. 295, 5785–5794.
793 https://doi.org/10.1074/jbc.RA119.012497
794 Alfadhli, A., Romanaggi, C., Barklis, R.L., Merutka, I., Bates, T.A., Tafesse, F.G., Barklis, E., 2021.
795 Capsid-specific nanobody effects on HIV-1 assembly and infectivity. Virology 562, 19–28.
796 https://doi.org/10.1016/j.virol.2021.07.001
797 Andersen, P., Andersen, A.B., Sørensen, A.L., Nagai, S., 1995. Recall of long-lived immunity to
798 Mycobacterium tuberculosis infection in mice. J Immunol 154, 3359–3372.
799 Andreu, N., Zelmer, A., Fletcher, T., Elkington, P.T., Ward, T.H., Ripoll, J., Parish, T., Bancroft, G.J.,
800 Schaible, U., Robertson, B.D., Wiles, S., 2010. Optimisation of Bioluminescent Reporters
801 for Use with Mycobacteria. PLoS One 5, e10777.
802 https://doi.org/10.1371/journal.pone.0010777
803 Augenstreich, J., Arbues, A., Simeone, R., Haanappel, E., Wegener, A., Sayes, F., Chevalier, F.L.,
804 Chalut, C., Malaga, W., Guilhot, C., Brosch, R., Astarie-Dequeker, C., 2017. ESX-1 and
805 phthiocerol dimycocerosates of Mycobacterium tuberculosis act in concert to cause
806 phagosomal rupture and host cell apoptosis. Cellular Microbiology 19, e12726.
807 https://doi.org/10.1111/cmi.12726
808 Augenstreich, J., Haanappel, E., Sayes, F., Simeone, R., Guillet, V., Mazeres, S., Chalut, C.,
809 Mourey, L., Brosch, R., Guilhot, C., Astarie-Dequeker, C., 2020. Phthiocerol
810 Dimycocerosates From Mycobacterium tuberculosis Increase the Membrane Activity of
811 Bacterial Effectors and Host Receptors. Frontiers in Cellular and Infection Microbiology
812 10.
813 Bachran, C., Schröder, M., Conrad, L., Cragnolini, J.J., Tafesse, F.G., Helming, L., Ploegh, H.L.,
814 Swee, L.K., 2017. The activity of myeloid cell-specific VHH immunotoxins is target-,
815 epitope-, subset- and organ dependent. Sci Rep 7, 17916. https://doi.org/10.1038/s41598-
816 017-17948-0
817 Behura, A., Mishra, Abtar, Chugh, S., Mawatwal, S., Kumar, A., Manna, D., Mishra, Amit, Singh,
818 R., Dhiman, R., 2019. ESAT-6 modulates Calcimycin-induced autophagy through
819 microRNA-30a in mycobacteria infected macrophages. Journal of Infection 79, 139–152.
820 https://doi.org/10.1016/j.jinf.2019.06.001
821 Bosserman, R.E., Nicholson, K.R., Champion, M.M., Champion, P.A., 2019. A New ESX-1
822 Substrate in Mycobacterium marinum That Is Required for Hemolysis but Not Host Cell
823 Lysis. J Bacteriol 201. https://doi.org/10.1128/JB.00760-18
824 Canton, J., Khezri, R., Glogauer, M., Grinstein, S., 2014. Contrasting phagosome pH regulation
825 and maturation in human M1 and M2 macrophages. Mol Biol Cell 25, 3330–3341.
826 https://doi.org/10.1091/mbc.E14-05-0967
827 Carlsson, F., Joshi, S.A., Rangell, L., Brown, E.J., 2009. Polar Localization of Virulence-Related
828 Esx-1 Secretion in Mycobacteria. PLOS Pathogens 5, e1000285.
829 https://doi.org/10.1371/journal.ppat.1000285
830 Chen, J.M., Boy-Röttger, S., Dhar, N., Sweeney, N., Buxton, R.S., Pojer, F., Rosenkrands, I., Cole,
831 S.T., 2012. EspD is critical for the virulence-mediating ESX-1 secretion system in
832 Mycobacterium tuberculosis. J Bacteriol 194, 884–893. https://doi.org/10.1128/JB.06417-
833 11
834 Chen, Y., Xiao, J., Li, Y., Xiao, Y., Xiong, Y., Liu, Y., Wang, S., Ji, P., Zhao, G., Shen, H., Lu, S.,
835 Fan, X., Wang, Y., 2019. Mycobacterial Lipoprotein Z Triggers Efficient Innate and
836 Adaptive Immunity for Protection Against Mycobacterium tuberculosis Infection. Frontiers
837 in Immunology 9.

838 Choi, H.-H., Shin, D.-M., Kang, G., Kim, K.-H., Park, J.B., Hur, G.M., Lee, H.-M., Lim, Y.-J., Park,
839 J.-K., Jo, E.-K., Song, C.-H., 2010. Endoplasmic reticulum stress response is involved in
840 Mycobacterium tuberculosis protein ESAT-6-mediated apoptosis. FEBS Letters 584,
841 2445–2454. https://doi.org/10.1016/j.febslet.2010.04.050
842 Clemmensen, H.S., Knudsen, N.P.H., Rasmussen, E.M., Winkler, J., Rosenkrands, I., Ahmad, A.,
843 Lillebaek, T., Sherman, D.R., Andersen, P.L., Aagaard, C., 2017. An attenuated
844 Mycobacterium tuberculosis clinical strain with a defect in ESX-1 secretion induces
845 minimal host immune responses and pathology. Scientific Reports 7, 46666.
846 https://doi.org/10.1038/srep46666
847 Collars, O.A., Jones, B.S., Hu, D.D., Weaver, S.D., Champion, M.M., Champion, P.A., 2023. An
848 N-acetyltransferase required for EsxA N-terminal protein acetylation and virulence in
849 Mycobacterium marinum. bioRxiv 2023.03.14.532585.
850 https://doi.org/10.1101/2023.03.14.532585
851 Conrad, W.H., Osman, M.M., Shanahan, J.K., Chu, F., Takaki, K.K., Cameron, J., Hopkinson-
852 Woolley, D., Brosch, R., Ramakrishnan, L., 2017. Mycobacterial ESX-1 secretion system
853 mediates host cell lysis through bacterium contact-dependent gross membrane
854 disruptions. Proc Natl Acad Sci U S A 114, 1371–1376.
855 https://doi.org/10.1073/pnas.1620133114
856 Cronin, R.M., Ferrell, M.J., Cahir, C.W., Champion, M.M., Champion, P.A., 2022. Proteo-genetic
857 analysis reveals clear hierarchy of ESX-1 secretion in Mycobacterium marinum. Proc Natl
858 Acad Sci U S A 119, e2123100119. https://doi.org/10.1073/pnas.2123100119
859 de Jonge, M.I., Pehau-Arnaudet, G., Fretz, M.M., Romain, F., Bottai, D., Brodin, P., Honoré, N.,
860 Marchal, G., Jiskoot, W., England, P., Cole, S.T., Brosch, R., 2007. ESAT-6 from
861 Mycobacterium tuberculosis dissociates from its putative chaperone CFP-10 under acidic
862 conditions and exhibits membrane-lysing activity. J Bacteriol 189, 6028–6034.
863 https://doi.org/10.1128/JB.00469-07
864 De Leon, J., Jiang, G., Ma, Y., Rubin, E., Fortune, S., Sun, J., 2012. Mycobacterium tuberculosis
865 ESAT-6 exhibits a unique membrane-interacting activity that is not found in its ortholog
866 from non-pathogenic Mycobacterium smegmatis. J Biol Chem 287, 44184–44191.
867 https://doi.org/10.1074/jbc.M112.420869
868 Dong, H., Jing, W., Runpeng, Z., Xuewei, X., Min, M., Ru, C., Yingru, X., Shengfa, N., Rongbo,
869 Z., 2016. ESAT6 inhibits autophagy flux and promotes BCG proliferation through MTOR.
870 Biochemical and Biophysical Research Communications 477, 195–201.
871 https://doi.org/10.1016/j.bbrc.2016.06.042
872 Eitson, J.L., Medeiros, J.J., Hoover, A.R., Srivastava, S., Roybal, K.T., Aínsa, J.A., Hansen, E.J.,
873 Gumbo, T., van Oers, N.S.C., 2012. Mycobacterial Shuttle Vectors Designed for High-
874 Level Protein Expression in Infected Macrophages. Appl Environ Microbiol 78, 6829–
875 6837. https://doi.org/10.1128/AEM.01674-12
876 Fan, Y., Tan, K., Chhor, G., Butler, E.K., Jedrzejczak, R.P., Missiakas, D., Joachimiak, A., 2015.
877 EsxB, a secreted protein from Bacillus anthracis forms two distinct helical bundles. Protein
878 Sci 24, 1389–1400. https://doi.org/10.1002/pro.2715
879 Frei, J.C., Lai, J.R., 2016. Protein and Antibody Engineering by Phage Display, in: Methods in
880 Enzymology. Elsevier, pp. 45–87. https://doi.org/10.1016/bs.mie.2016.05.005
881 Gallegos, A.M., Pamer, E.G., Glickman, M.S., 2008. Delayed protection by ESAT-6–specific
882 effector CD4+ T cells after airborne M. tuberculosis infection. Journal of Experimental
883 Medicine 205, 2359–2368. https://doi.org/10.1084/jem.20080353
884 García-Nafría, J., Watson, J.F., Greger, I.H., 2016. IVA cloning: A single-tube universal cloning
885 system exploiting bacterial In Vivo Assembly. Sci Rep 6, 27459.
886 https://doi.org/10.1038/srep27459

887 Gey van Pittius, N.C., Gamieldien, J., Hide, W., Brown, G.D., Siezen, R.J., Beyers, A.D., 2001.
888 The ESAT-6 gene cluster of Mycobacterium tuberculosis and other high G+C Gram-
889 positive bacteria. Genome Biol 2, research0044.1-research0044.18.
890 Giglione, C., Boularot, A., Meinnel, T., 2004. Protein N-terminal methionine excision. Cell Mol Life
891 Sci 61, 1455–1474. https://doi.org/10.1007/s00018-004-3466-8
892 Guimaraes, C.P., Witte, M.D., Theile, C.S., Bozkurt, G., Kundrat, L., Blom, A.E.M., Ploegh, H.L.,
893 2013. Site-specific C-terminal and internal loop labeling of proteins using sortase-
894 mediated reactions. Nat Protoc 8, 1787–1799. https://doi.org/10.1038/nprot.2013.101
895 Harris, N.J., Jenkins, M.L., Nam, S.-E., Rathinaswamy, M.K., Parson, M.A.H., Ranga-Prasad, H.,
896 Dalwadi, U., Moeller, B.E., Sheeky, E., Hansen, S.D., Yip, C.K., Burke, J.E., 2023.
897 Allosteric activation or inhibition of PI3Kγ mediated through conformational changes in the
898 p110γ helical domain. Elife 12, RP88058. https://doi.org/10.7554/eLife.88058
899 Harrison, D.E., Astle, C.M., Niazi, M.K.K., Major, S., Beamer, G.L., 2014. Genetically diverse mice
900 are novel and valuable models of age-associated susceptibility to Mycobacterium
901 tuberculosis. Immunity & Ageing 11, 24. https://doi.org/10.1186/s12979-014-0024-6
902 Hirel, P.H., Schmitter, M.J., Dessen, P., Fayat, G., Blanquet, S., 1989. Extent of N-terminal
903 methionine excision from Escherichia coli proteins is governed by the side-chain length of
904 the penultimate amino acid. Proceedings of the National Academy of Sciences 86, 8247–
905 8251. https://doi.org/10.1073/pnas.86.21.8247
906 Hoogenboom, H.R., Griffiths, A.D., Johnson, K.S., Chiswell, D.J., Hudson, P., Winter, G., 1991.
907 Multi-subunit proteins on the surface of filamentous phage: methodologies for displaying
908 antibody (Fab) heavy and light chains. Nucleic Acids Res 19, 4133–4137.
909 https://doi.org/10.1093/nar/19.15.4133
910 Houben, D., Demangel, C., van Ingen, J., Perez, J., Baldeon, L., Abdallah, A.M., Caleechurn, L.,
911 Bottai, D., van Zon, M., de Punder, K., van der Laan, T., Kant, A., Bossers-de Vries, R.,
912 Willemsen, P., Bitter, W., van Soolingen, D., Brosch, R., van der Wel, N., Peters, P.J.,
913 2012. ESX-1-mediated translocation to the cytosol controls virulence of mycobacteria. Cell
914 Microbiol 14, 1287–98. https://doi.org/10.1111/j.1462-5822.2012.01799.x
915 Houben, R.M.G.J., Dodd, P.J., 2016. The Global Burden of Latent Tuberculosis Infection: A Re-
916 estimation Using Mathematical Modelling. PLOS Medicine 13, e1002152.
917 https://doi.org/10.1371/journal.pmed.1002152
918 Jang, A.R., Choi, J.H., Shin, S.J., Park, J.H., 2018. Mycobacterium tuberculosis ESAT6 induces
919 IFN-beta gene expression in Macrophages via TLRs-mediated signaling. Cytokine 104,
920 104–109. https://doi.org/10.1016/j.cyto.2017.10.006
921 Karki, C., Xian, Y., Xie, Y., Sun, S., Lopez-Hernandez, A.E., Juarez, B., Wang, J., Sun, J., Li, L.,
922 2020. A computational model of ESAT-6 complex in membrane. J Theor Comput Chem
923 19, 2040002. https://doi.org/10.1142/s0219633620400027
924 Kinhikar, A.G., Verma, I., Chandra, D., Singh, K.K., Weldingh, K., Andersen, P., Hsu, T., Jacobs,
925 W.R., Laal, S., 2010. Potential role for ESAT6 in dissemination of M. tuberculosis via
926 human lung epithelial cells. Mol Microbiol 75, 92–106. https://doi.org/10.1111/j.1365-
927 2958.2009.06959.x
928 Koo, I.C., Wang, C., Raghavan, S., Morisaki, J.H., Cox, J.S., Brown, E.J., 2008. ESX-1-dependent
929 cytolysis in lysosome secretion and inflammasome activation during mycobacterial
930 infection. Cell Microbiol 10, 1866–1878. https://doi.org/10.1111/j.1462-5822.2008.01177.x
931 Koyuncu, D., Niazi, M.K.K., Tavolara, T., Abeijon, C., Ginese, M.L., Liao, Y., Mark, C., Specht, A.,
932 Gower, A.C., Restrepo, B.I., Gatti, D.M., Kramnik, I., Gurcan, M., Yener, B., Beamer, G.,
933 2021. CXCL1: A new diagnostic biomarker for human tuberculosis discovered using
934 Diversity Outbred mice. PLOS Pathogens 17, e1009773.
935 https://doi.org/10.1371/journal.ppat.1009773
936 Kumar, P., Agarwal, R., Siddiqui, I., Vora, H., Das, G., Sharma, P., 2012. ESAT6 differentially
937 inhibits IFN-γ-inducible class II transactivator isoforms in both a TLR2-dependent and -

independent manner. Immunology & Cell Biology 90, 411–420. https://doi.org/10.1038/icb.2011.54

Leddy, O., White, F.M., Bryson, B.D., 2023. Immunopeptidomics reveals determinants of Mycobacterium tuberculosis antigen presentation on MHC class I. eLife 12, e84070. https://doi.org/10.7554/eLife.84070

Lienard, J., Nobs, E., Lovins, V., Movert, E., Valfridsson, C., Carlsson, F., 2020. The Mycobacterium marinum ESX-1 system mediates phagosomal permeabilization and type I interferon production via separable mechanisms. Proc Natl Acad Sci U S A 117, 1160–1166. https://doi.org/10.1073/pnas.1911646117

Lightbody, K.L., Ilghari, D., Waters, L.C., Carey, G., Bailey, M.A., Williamson, R.A., Renshaw, P.S., Carr, M.D., 2008. Molecular features governing the stability and specificity of functional complex formation by Mycobacterium tuberculosis CFP-10/ESAT-6 family proteins. J Biol Chem 283, 17681–17690. https://doi.org/10.1074/jbc.M800123200

Lim, Y.-J., Yi, M.-H., Choi, J.-A., Lee, J., Han, J.-Y., Jo, S.-H., Oh, S.-M., Cho, H.J., Kim, D.W., Kang, M.-W., Song, C.-H., 2016. Roles of endoplasmic reticulum stress-mediated apoptosis in M1-polarized macrophages during mycobacterial infections. Sci Rep 6, 37211. https://doi.org/10.1038/srep37211

López-Jiménez, A.T., Cardenal-Muñoz, E., Leuba, F., Gerstenmaier, L., Barisch, C., Hagedorn, M., King, J.S., Soldati, T., 2018. The ESCRT and autophagy machineries cooperate to repair ESX-1-dependent damage at the Mycobacterium-containing vacuole but have opposite impact on containing the infection. PLOS Pathogens 14, e1007501. https://doi.org/10.1371/journal.ppat.1007501

Maass, D.R., Sepulveda, J., Pernthaner, A., Shoemaker, C.B., 2007. Alpaca (Lama pacos) as a convenient source of recombinant camelid heavy chain antibodies (VHHs). J Immunol Methods 324, 13–25. https://doi.org/10.1016/j.jim.2007.04.008

MacMicking, J.D., Taylor, G.A., McKinney, J.D., 2003. Immune Control of Tuberculosis by IFN-γ-Inducible LRG-47. Science 302, 654–659. https://doi.org/10.1126/science.1088063

Martin, C.J., Booty, M.G., Rosebrock, T.R., Nunes-Alves, C., Desjardins, D.M., Keren, I., Fortune, S.M., Remold, H.G., Behar, S.M., 2012. Efferocytosis is an innate antibacterial mechanism. Cell Host Microbe 12, 289–300. https://doi.org/10.1016/j.chom.2012.06.010

Masson, G.R., Burke, J.E., Ahn, N.G., Anand, G.S., Borchers, C., Brier, S., Bou-Assaf, G.M., Engen, J.R., Englander, S.W., Faber, J., Garlish, R., Griffin, P.R., Gross, M.L., Guttman, M., Hamuro, Y., Heck, A.J.R., Houde, D., Iacob, R.E., Jørgensen, T.J.D., Kaltashov, I.A., Klinman, J.P., Konermann, L., Man, P., Mayne, L., Pascal, B.D., Reichmann, D., Skehel, M., Snijder, J., Strutzenberg, T.S., Underbakke, E.S., Wagner, C., Wales, T.E., Walters, B.T., Weis, D.D., Wilson, D.J., Wintrode, P.L., Zhang, Z., Zheng, J., Schriemer, D.C., Rand, K.D., 2019. Recommendations for performing, interpreting and reporting hydrogen deuterium exchange mass spectrometry (HDX-MS) experiments. Nat Methods 16, 595–602. https://doi.org/10.1038/s41592-019-0459-y

Mba Medie, F., Champion, M.M., Williams, E.A., Champion, P.A.D., 2014. Homeostasis of N-α-Terminal Acetylation of EsxA Correlates with Virulence in Mycobacterium marinum. Infect Immun 82, 4572–4586. https://doi.org/10.1128/IAI.02153-14

McIlvaine, T.C., 1921. A BUFFER SOLUTION FOR COLORIMETRIC COMPARISON. Journal of Biological Chemistry 49, 183–186. https://doi.org/10.1016/S0021-9258(18)86000-8

Meerbrey, K.L., Hu, G., Kessler, J.D., Roarty, K., Li, M.Z., Fang, J.E., Herschkowitz, J.I., Burrows, A.E., Ciccia, A., Sun, T., Schmitt, E.M., Bernardi, R.J., Fu, X., Bland, C.S., Cooper, T.A., Schiff, R., Rosen, J.M., Westbrook, T.F., Elledge, S.J., 2011. The pINDUCER lentiviral toolkit for inducible RNA interference in vitro and in vivo. Proc Natl Acad Sci U S A 108, 3665–3670. https://doi.org/10.1073/pnas.1019736108

Mukherjee, P., Dutta, M., Datta, P., Dasgupta, A., Pradhan, R., Pradhan, M., Kundu, M., Basu, J., Chakrabarti, P., 2007. The RD1-encoded antigen Rv3872 of Mycobacterium tuberculosis

989 as a potential candidate for serodiagnosis of tuberculosis. Clinical Microbiology and
990 Infection 13, 146–152. https://doi.org/10.1111/j.1469-0691.2006.01660.x
991 Niazi, M.K.K., Dhulekar, N., Schmidt, D., Major, S., Cooper, R., Abeijon, C., Gatti, D.M., Kramnik,
992 I., Yener, B., Gurcan, M., Beamer, G., 2015. Lung necrosis and neutrophils reflect common
993 pathways of susceptibility to Mycobacterium tuberculosis in genetically diverse, immune-
994 competent mice. Dis Model Mech 8, 1141–1153. https://doi.org/10.1242/dmm.020867
995 Niekamp, P., Guzman, G., Leier, H.C., Rashidfarrokhi, A., Richina, V., Pott, F., Barisch, C.,
996 Holthuis, J.C.M., Tafesse, F.G., 2021. Sphingomyelin Biosynthesis Is Essential for
997 Phagocytic Signaling during Mycobacterium tuberculosis Host Cell Entry. mBio 12,
998 e03141-20. https://doi.org/10.1128/mBio.03141-20
999 Okkels, L.M., Müller, E.-C., Schmid, M., Rosenkrands, I., Kaufmann, S.H.E., Andersen, P.,
1000 Jungblut, P.R., 2004. CFP10 discriminates between nonacetylated and acetylated ESAT-
1001 6 of Mycobacterium tuberculosis by differential interaction. PROTEOMICS 4, 2954–2960.
1002 https://doi.org/10.1002/pmic.200400906
1003 Osman, M.M., Shanahan, J.K., Chu, F., Takaki, K.K., Pinckert, M.L., Pagán, A.J., Brosch, R.,
1004 Conrad, W.H., Ramakrishnan, L., 2022. The C terminus of the mycobacterium ESX-1
1005 secretion system substrate ESAT-6 is required for phagosomal membrane damage and
1006 virulence. Proc Natl Acad Sci U S A 119, e2122161119.
1007 https://doi.org/10.1073/pnas.2122161119
1008 Pathak, S.K., Basu, S., Basu, K.K., Banerjee, A., Pathak, S., Bhattacharyya, A., Kaisho, T., Kundu,
1009 M., Basu, J., 2007. Direct extracellular interaction between the early secreted antigen
1010 ESAT-6 of Mycobacterium tuberculosis and TLR2 inhibits TLR signaling in macrophages.
1011 Nat Immunol 8, 610–618. https://doi.org/10.1038/ni1468
1012 Peng, H., Wang, X., Barnes, P.F., Tang, H., Townsend, J.C., Samten, B., 2011. The
1013 Mycobacterium tuberculosis Early Secreted Antigenic Target of 6 kDa Inhibits T Cell
1014 Interferon-γ Production through the p38 Mitogen-activated Protein Kinase Pathway. J Biol
1015 Chem 286, 24508–24518. https://doi.org/10.1074/jbc.M111.234062
1016 Perez-Riverol, Y., Bai, J., Bandla, C., García-Seisdedos, D., Hewapathirana, S., Kamatchinathan,
1017 S., Kundu, D.J., Prakash, A., Frericks-Zipper, A., Eisenacher, M., Walzer, M., Wang, S.,
1018 Brazma, A., Vizcaíno, J.A., 2022. The PRIDE database resources in 2022: a hub for mass
1019 spectrometry-based proteomics evidences. Nucleic Acids Res 50, D543–D552.
1020 https://doi.org/10.1093/nar/gkab1038
1021 Popp, M.W., Antos, J.M., Ploegh, H.L., 2009. Site-specific protein labeling via sortase-mediated
1022 transpeptidation. Curr Protoc Protein Sci Chapter 15, Unit 15 3.
1023 https://doi.org/10.1002/0471140864.ps1503s56
1024 Poulsen, C., Panjikar, S., Holton, S.J., Wilmanns, M., Song, Y.-H., 2014. WXG100 Protein
1025 Superfamily Consists of Three Subfamilies and Exhibits an α-Helical C-Terminal
1026 Conserved Residue Pattern. PLOS ONE 9, e89313.
1027 https://doi.org/10.1371/journal.pone.0089313
1028 Rathinaswamy, M.K., Fleming, K.D., Dalwadi, U., Pardon, E., Harris, N.J., Yip, C.K., Steyaert, J.,
1029 Burke, J.E., 2021. HDX-MS-optimized approach to characterize nanobodies as tools for
1030 biochemical and structural studies of class IB phosphoinositide 3-kinases. Structure 29,
1031 1371-1381.e6. https://doi.org/10.1016/j.str.2021.07.002
1032 Refai, A., Haoues, M., Othman, H., Barbouche, M.R., Moua, P., Bondon, A., Mouret, L., Srairi-
1033 Abid, N., Essafi, M., 2015. Two distinct conformational states of Mycobacterium
1034 tuberculosis virulent factor early secreted antigenic target 6 kDa are behind the
1035 discrepancy around its biological functions. The FEBS Journal 282, 4114–4129.
1036 https://doi.org/10.1111/febs.13408
1037 Renshaw, P.S., Lightbody, K.L., Veverka, V., Muskett, F.W., Kelly, G., Frenkiel, T.A., Gordon, S.V.,
1038 Hewinson, R.G., Burke, B., Norman, J., Williamson, R.A., Carr, M.D., 2005. Structure and

function of the complex formed by the tuberculosis virulence factors CFP-10 and ESAT-6. The EMBO Journal 24, 2491–2498. https://doi.org/10.1038/sj.emboj.7600732

Renshaw, P.S., Panagiotidou, P., Whelan, A., Gordon, S.V., Hewinson, R.G., Williamson, R.A., Carr, M.D., 2002. Conclusive Evidence That the Major T-cell Antigens of theMycobacterium tuberculosis Complex ESAT-6 and CFP-10 Form a Tight, 1:1 Complex and Characterization of the Structural Properties of ESAT-6, CFP-10, and the ESAT-6·CFP-10 Complex: IMPLICATIONS FOR PATHOGENESIS AND VIRULENCE *. Journal of Biological Chemistry 277, 21598–21603. https://doi.org/10.1074/jbc.M201625200

Romagnoli, A., Etna, M.P., Giacomini, E., Pardini, M., Remoli, M.E., Corazzari, M., Falasca, L., Goletti, D., Gafa, V., Simeone, R., Delogu, G., Piacentini, M., Brosch, R., Fimia, G.M., Coccia, E.M., 2012. ESX-1 dependent impairment of autophagic flux by Mycobacterium tuberculosis in human dendritic cells. Autophagy 8, 1357–1370. https://doi.org/10.4161/auto.20881

Sanchez, K.G., Ferrell, M.J., Chirakos, A.E., Nicholson, K.R., Abramovitch, R.B., Champion, M.M., Champion, P.A., 2020. EspM Is a Conserved Transcription Factor That Regulates Gene Expression in Response to the ESX-1 System. mBio 11. https://doi.org/10.1128/mBio.02807-19

Santucci, P., Aylan, B., Botella, L., Bernard, E.M., Bussi, C., Pellegrino, E., Athanasiadi, N., Gutierrez, M.G., 2022. Visualizing Pyrazinamide Action by Live Single-Cell Imaging of Phagosome Acidification and Mycobacterium tuberculosis pH Homeostasis. mBio 13, e00117-22. https://doi.org/10.1128/mbio.00117-22

Schnettger, L., Rodgers, A., Repnik, U., Lai, R.P., Pei, G., Verdoes, M., Wilkinson, R.J., Young, D.B., Gutierrez, M.G., 2017. A Rab20-Dependent Membrane Trafficking Pathway Controls M. tuberculosis Replication by Regulating Phagosome Spaciousness and Integrity. Cell Host & Microbe 21, 619-628.e5. https://doi.org/10.1016/j.chom.2017.04.004

Smith, J., Manoranjan, J., Pan, M., Bohsali, A., Xu, J., Liu, J., McDonald, K.L., Szyk, A., LaRonde-LeBlanc, N., Gao, L.-Y., 2008. Evidence for Pore Formation in Host Cell Membranes by ESX-1-Secreted ESAT-6 and Its Role in Mycobacterium marinum Escape from the Vacuole. Infect Immun 76, 5478–5487. https://doi.org/10.1128/IAI.00614-08

Sørensen, A.L., Nagai, S., Houen, G., Andersen, P., Andersen, A.B., 1995. Purification and characterization of a low-molecular-mass T-cell antigen secreted by Mycobacterium tuberculosis. Infect Immun 63, 1710–1717. https://doi.org/10.1128/iai.63.5.1710-1717.1995

Sreejit, G., Ahmed, A., Parveen, N., Jha, V., Valluri, V.L., Ghosh, S., Mukhopadhyay, S., 2014. The ESAT-6 Protein of Mycobacterium tuberculosis Interacts with Beta-2-Microglobulin (β2M) Affecting Antigen Presentation Function of Macrophage. PLOS Pathogens 10, e1004446. https://doi.org/10.1371/journal.ppat.1004446

Stariha, J.T.B., Hoffmann, R.M., Hamelin, D.J., Burke, J.E., 2021. Probing Protein-Membrane Interactions and Dynamics Using Hydrogen-Deuterium Exchange Mass Spectrometry (HDX-MS). Methods Mol Biol 2263, 465–485. https://doi.org/10.1007/978-1-0716-1197-5_22

Stavri, H., Bucurenci, N., Ulea, I., Costache, A., Popa, L., Popa, M.I., 2012. Use of recombinant purified protein derivative (PPD) antigens as specific skin test for tuberculosis. Indian Journal of Medical Research 136, 799.

Stirling, D.R., Swain-Bowden, M.J., Lucas, A.M., Carpenter, A.E., Cimini, B.A., Goodman, A., 2021. CellProfiler 4: improvements in speed, utility and usability. BMC Bioinformatics 22, 433. https://doi.org/10.1186/s12859-021-04344-9

Tak, U., Dokland, T., Niederweis, M., 2021. Pore-forming Esx proteins mediate toxin secretion by Mycobacterium tuberculosis. Nat Commun 12. https://doi.org/10.1038/s41467-020-20533-1

1089 Vandal, O.H., Pierini, L.M., Schnappinger, D., Nathan, C.F., Ehrt, S., 2008. A membrane protein
1090 preserves intrabacterial pH in intraphagosomal Mycobacterium tuberculosis. Nat Med 14,
1091 849–854. https://doi.org/10.1038/nm.1795
1092 Vesosky, B., Rottinghaus, E.K., Stromberg, P., Turner, J., Beamer, G., 2010. CCL5 participates in
1093 early protection against Mycobacterium tuberculosis. Journal of Leukocyte Biology 87,
1094 1153–1165. https://doi.org/10.1189/jlb.1109742
1095 Weinstein, J.B., Bates, T.A., Leier, H.C., McBride, S.K., Barklis, E., Tafesse, F.G., 2022. A potent
1096 alpaca-derived nanobody that neutralizes SARS-CoV-2 variants. iScience 25, 103960.
1097 https://doi.org/10.1016/j.isci.2022.103960
1098 Woolhiser, L., Tamayo, M.H., Wang, B., Gruppo, V., Belisle, J.T., Lenaerts, A.J., Basaraba, R.J.,
1099 Orme, I.M., 2007. In Vivo Adaptation of the Wayne Model of Latent Tuberculosis. Infection
1100 and Immunity 75, 2621–2625. https://doi.org/10.1128/iai.00918-06
1101 World Health Organization, 2022. Global tuberculosis report 2022. World Health Organization,
1102 Geneva.
1103 Xiao, Y., Sha, W., Tian, Z., Chen, Y., Ji, P., Sun, Q., Wang, H., Wang, S., Fang, Y., Wen, H.-L.,
1104 Zhao, H., Lu, J., Xiao, H., Fan, X., Shen, H., Wang, Y., 2016. Adenylate kinase: a novel
1105 antigen for immunodiagnosis and subunit vaccine against tuberculosis. J Mol Med 94,
1106 823–834. https://doi.org/10.1007/s00109-016-1392-5
1107 Yabaji, S.M., Dhamija, E., Mishra, A.K., Srivastava, K.K., 2020. ESAT-6 regulates autophagous
1108 response through SOD-2 and as a result induces intracellular survival of Mycobacterium
1109 bovis BCG. Biochimica et Biophysica Acta (BBA) - Proteins and Proteomics 1868, 140470.
1110 https://doi.org/10.1016/j.bbapap.2020.140470
1111 Yang, C.-S., Lee, J.-S., Lee, H.-M., Sun Shim, T., Woong Son, J., Jung, S.-S., Kim, J.-S., Song,
1112 C.-H., Kim, H.-J., Jo, E.-K., 2008. Differential cytokine levels and immunoreactivities
1113 against Mycobacterium tuberculosis antigens between tuberculous and malignant
1114 effusions. Respiratory Medicine 102, 280–286.
1115 https://doi.org/10.1016/j.rmed.2007.08.016
1116 Yang, S., Li, F., Jia, S., Zhang, K., Jiang, W., Shang, Y., Chang, K., Deng, S., Chen, M., 2015.
1117 Early secreted antigen ESAT-6 of Mycobacterium Tuberculosis promotes apoptosis of
1118 macrophages via targeting the microRNA155-SOCS1 interaction. Cell. Physiol. Biochem.
1119 35, 1276–1288. https://doi.org/10.1159/000373950
1120